Journal of Instrumentation

EXILL—a high-efficiency, high-resolution setup for γ-spectroscopy at an intense cold neutron beam facility

Jinst

Published by IOP Publishing for Sissa Medialab

Received: *August 21, 2017*
Accepted: *September 26, 2017*
Published: *November 7, 2017*

EXILL — a high-efficiency, high-resolution setup for γ-spectroscopy at an intense cold neutron beam facility

EXILL-Core collaboration

M. Jentschel,[a,1] A. Blanc,[a] G. de France,[b] U. Köster,[a] S. Leoni,[c] P. Mutti,[a] G. Simpson,[d] T. Soldner,[a] C. Ur,[e,f] W. Urban[a,g]
and
S. Ahmed,[h] A. Astier,[i] L. Augey,[j] T. Back,[k] P. Bączyk,[g] A. Bajoga,[l] D. Balabanski,[m,f] T. Belgya,[n] G. Benzoni,[c] C. Bernards,[o] D.C. Biswas,[p] G. Bocchi,[c] S. Bottoni,[c] R. Britton,[l] B. Bruyneel,[q] J. Burnett,[r] R.B. Cakirli,[s] R. Carroll,[l] W. Catford,[l] B. Cederwall,[k] I. Celikovic,[b] N. Cieplicka-Oryń,czak,[t] E. Clement,[b] N. Cooper,[o] F. Crespi,[c] M. Csatlos,[u] D. Curien,[v] M. Czerwiński,[g] L.S. Danu,[p] A. Davies,[l] F. Didierjean,[v] F. Drouet,[w] G. Duchê,ne,[v] C. Ducoin,[j] K. Eberhardt,[x] S. Erturk,[y] L.M. Fraile,[z] A. Gottardo,[aa] L. Grente,[q] L. Grocutt,[ab] C. Guerrero,[ac] D. Guinet,[j] A.-L. Hartig,[ad] C. Henrich,[ad] A. Ignatov,[ad] S. Ilieva,[ad] D. Ivanova,[ae] B.V. John,[p] R. John,[af] J. Jolie,[h] S. Kisyov,[ae] M. Krticka,[at] T. Konstantinopoulos,[i] A. Korgul,[g] A. Krasznahorkay,[u] T. Kröll,[ad] J. Kurpeta,[g] I. Kuti,[u] S. Lalkovski,[l] C. Larijani,[ag] R. Leguillon,[ah] R. Lica,[ai] O. Litaize,[aj] R. Lozeva,[i,v] C. Magron,[ak] C. Mancuso,[j] E. Ruiz Martinez,[a] R. Massarczyk,[af] C. Mazzocchi,[g] B. Melon,[al,am] D. Mengoni,[e] C. Michelagnoli,[a,b] B. Million,[c] C. Mokry,[x] S. Mukhopadhyay,[p] K. Mulholland,[ab] A. Nannini,[am] D.R. Napoli,[aa] B. Olaizola,[z] R. Orlandi,[ah] Z. Patel,[l] V. Paziy,[z] C. Petrache,[i] M. Pfeiffer,[h] N. Pietralla,[ad] Z. Podolyak,[l] M. Ramdhane,[an] N. Redon,[j] P. Regan,[l] J.M. Regis,[h] D. Regnier,[aj] R. J. Oliver,[ao] M. Rudigier,[l] J. Runke,[x] T. Rząca-Urban,[g] N. Saed-Samii,[h] M.D. Salsac,[q] M. Scheck,[ab] R. Schwengner,[af] L. Sengele,[v] P. Singh,[ap] J. Smith,[ab] O. Stezowski,[j] B. Szpak,[t] T. Thomas,[h] M. Thürauf,[ad] J. Timar,[u] A. Tom,[l] I. Tomandl,[aq] T. Tornyi,[u] C. Townsley,[ar] A. Tuerler,[as] S. Valenta,[at] A. Vancraeyenest,[w] V. Vandone,[c] J. Vanhoy,[au] V. Vedia,[z] N. Warr,[h] V. Werner,[o,ad] D. Wilmsen,[b] E. Wilson,[aa] T. Zerrouki,[i] and M. Zielinska[q]

[a] *Institut Laue-Langevin, 71 avenue des Martyrs, 38042 Grenoble Cedex 9, France*
[b] *GANIL, Bvd. Becquerel, BP 55027, 14076 Caen Cedex 05, France*
[c] *Dipartimento di Fisica, Universita di Milano, Via Celoria 16, 20133 Milano, Italy*
[d] *LPSC, Université Grenoble Alpes, 38026 Grenoble Cedex, France*
[e] *Dipartimento di Fisica, Universita di Padova, Via F. Marzolo 8, 35131 Padova, Italy*
[f] *ELI-NP, National, IFIN-HH30, Reactorului, 077125 Bucharest-Magurele, Romania*

[1] Corresponding author.

https://doi.org/10.1088/1748-0221/12/11/P11003

2017 JINST 12 P11003

[g] Faculty of Physics, University of Warsaw, ul. Pasteura 5, 02-093, Warszawa, Poland
[h] IKP, University Cologne, Zülpicher Str. 77, 50937 Cologne, Germany
[i] CSNSM, CNRS-IN2P3, Université Paris-Saclay, 91405 Orsay Cedex, France
[j] IPN, Lyon Université Claude Bernard, 43 Blvd. du 11 Nov. 1918, 69622 Villeurbanne, France
[k] Physics Department, KTH, Roslagstullsbacken 21, 100 44 Stockholm, Sweden
[l] Department of Physics, University of Surrey, Surrey GU2 5XH Guildford, U.K.
[m] INRNE-Sofia, 72 Tzarigradsko Shaussee, 1784 Sofia, Bulgaria
[n] Hungarian Academy of Sciences CER, Konkoly T. st. 29-33, 1121 Budapest, Hungary
[o] Department of Physics, Yale University, P.O. Box 208120, CT 06520-8120 New Haven, U.S.A.
[p] Nuclear Physics Division, Bhabha Atomic Research Centre, Trombay, 400 085 Mumbai, India
[q] DSM/IRFU/SPHN CEA Saclay ORME des Merisiers, Bat. 703, 91191 Gif-sur-Yvette, France
[r] AWE PLC, Aldermaston, RG7 4PR Reading, U.K.
[s] Department of Physics, Istanbul University, Vezneciler, 34134 Istanbul, Turkey
[t] Institute of Nuclear Physics Polish Academy of Sciences, PL-31342 Krakow, Poland
[u] Institute for Nuclear Research, Hungarian Academy of Sciences, 4001 Debrecen, Hungary
[v] Université de Strasbourg, CNRS, IPHC UMR 7178, F-67000 Strasbourg, France
[w] INPG - PHELMA, 3 Parvis Louis Néel BP 257 - CEDEX 1, 38000 Grenoble, France
[x] Institut für Kernchemie, Universität Mainz, Fritz-Strassmann-Weg 2, 55128 Mainz, Germany
[y] Nigde University, Merkez Yerleske Bor Yolu Üzeri, 51240 Nigde, Turkey
[z] Universidad Complutense, Grupo de Fisica Nuclear, Fisicas Avda. Complutense, 28040 Madrid, Spain
[aa] INFN - Laboratori Nazionali di Legnaro, Vialle dell Universita 2, 35020 Legnaro, Italy
[ab] University of the West of Scotland, High Street, PA1 2BE Paisley, U.K.
[ac] CERN, 1211 Geneve 23, Switzerland
[ad] IKP, TU Darmstadt, Schlossgartenstr. 9, 64289 Darmstadt, Germany
[ae] Faculty of Physics, University of Sofia, 5 James Bourchier Blvd, 1126 Sofia, Bulgaria
[af] Helmholtz-Zentrum Dresden-Rossendorf, P.O. Box 510 119, 01314 Dresden, Germany
[ag] National Physics Laboratory, Teddington Queens Road, Middlesex Teddington, U.K.
[ah] JAEA, Tokai Shirakata-Shirane 2-4 Tokai, Naka 319-1195 Ibaraki, Japan
[ai] IFIN HH, Bucharest str. Atomistilor 407, P.O. Box MG-6, 76900 Bucharest, Romania
[aj] CEA Cadarache, 13108 Saint-Paul-lez-Durance, France
[ak] CENBG Bordeaux, Université de Bordeaux, 1 Le Haut Vigneau, 33170 Gradignan, France
[al] Dipartimento di Fisica e Astronomia, Università di Firenze,
Via G. Sansone 1 50019 Sesto Fiorentino - Firenze, Italy
[am] INFN Sezione di Firenze, Via G. Sansone 1, 50019 Sesto Fiorentino, Italy
[an] LPSC Grenoble, 53 Avenue des Martyrs, 38026 Grenoble, France
[ao] University of Brighton, School of Environment and Technology, Lewes Road BN2 4GJ Brighton
[ap] TATA Institute of Fundamental Research, Homi Bhabha Road, Colaba, 400 005 Mumbai, India
[aq] Nuclear Physics Institute, ASCR, Rez ASCR, 250 68 REZ, Czech Republic
[ar] School of Science and Technology, University Sussex, Falmer, BN1 9QJ Brighton, U.K.
[as] Department of Chemistry and Biochemistry, University of Bern, Freiestrasse 3, 3012 Bern, Switzerland
[at] Faculty of Mathematics and Physics, Prague Charles University,
Ke Karlovu 5, 121 16 Praha, Czech Republic
[au] US Naval Academy, Department of Physics, 572C Holloway Road, 21402 Annapolis, Maryland, U.S.A.

E-mail: jentsch@ill.fr

2017 JINST 12 P11003

Abstract: In the EXILL campaign a highly efficient array of high purity germanium (HPGe) detectors was operated at the cold neutron beam facility PF1B of the Institut Laue-Langevin (ILL) to carry out nuclear structure studies, via measurements of γ-rays following neutron-induced capture and fission reactions. The setup consisted of a collimation system producing a pencil beam with a thermal capture equivalent flux of about 10^8 n s^{-1}cm^{-2} at the target position and negligible neutron halo. The target was surrounded by an array of eight to ten anti-Compton shielded EXOGAM Clover detectors, four to six anti-Compton shielded large coaxial GASP detectors and two standard Clover detectors. For a part of the campaign the array was combined with 16 $LaBr_3$:(Ce) detectors from the FATIMA collaboration. The detectors were arranged in an array of rhombicuboctahedron geometry, providing the possibility to carry out very precise angular correlation and directional-polarization correlation measurements. The triggerless acquisition system allowed a signal collection rate of up to 6×10^5 Hz. The data allowed to set multi-fold coincidences to obtain decay schemes and in combination with the FATIMA array of $LaBr_3$:(Ce) detectors to analyze half-lives of excited levels in the pico- to microsecond range. Precise energy and efficiency calibrations of EXILL were performed using standard calibration sources of ^{133}Ba, ^{60}Co and ^{152}Eu as well as data from the reactions ^{27}Al(n,γ)^{28}Al and ^{35}Cl(n, γ)^{36}Cl in the energy range from 30 keV up to 10 MeV.

Keywords: Instrumentation for neutron sources; Gamma detectors (scintillators, CZT, HPG, HgI etc); Spectrometers

2017 JINST 12 P11003

Contents

1 Introduction **1**

2 The cold neutron beam facility PF1B and the neutron collimation system **4**

3 The target chamber **6**

4 Targets **8**
4.1 Stable targets 8
4.2 Radioactive targets 9

5 Detectors **11**

6 The digital data acquisition system **13**

7 Key performances **14**
7.1 Alignments and calibrations 15
7.1.1 Energy alignments and calibrations 15
7.1.2 Efficiency calibration 17
7.1.3 Time alignments and calibrations 19
7.2 Angular correlations 21

8 Summary and perspectives **26**

2017 JINST 12 P11003

1 Introduction

The use of high-purity germanium (HPGe) detectors combined to efficient arrays covering a substantial solid angle became a commonly used tool in nuclear spectroscopy since the 1980s [1]. Due to the high energy resolution and the possibility to build coincidences it is possible to understand even complex level schemes or to obtain high isotopic selectivity. Information on angular correlations or polarisation of γ-ray transitions can be obtained, providing the possibility to assign spin and parities to nuclear states. The only HPGe-detector arrays used so far at a neutron beam were limited to an array of 16 small Ge-detectors with 25% relative efficiency [2] or small assemblies of up to 8 large-volume Ge detectors [3, 4]. One reason lies probably in the limited availability of intense neutron beams for the nuclear physics community. Another reason is the fact that the high selectivity of a detector array requires sufficiently clean background conditions, which can turn out to be a non-trivial task in a neutron research facility. The study of neutron-capture induced reactions represents certainly an interesting field for nuclear structure physics. Even more interest comes from the possibility to carry out prompt γ-spectroscopy on fission products produced in reactions such as ^{235}U(n,f) or ^{241}Pu(n,f). The importance of fission product studies with HPGe-arrays has been

successfully demonstrated in the past by experiments with spontaneous fission sources such as ^{252}Cf and ^{248}Cm using the detector arrays EUROGAM/EUROBALL [5] and GAMMASPHERE [6, 7]. Neutron induced fission is a very effective way to produce neutron-rich nuclei in the mass range 85 <A< 160. Figure 1 compares the fission fragment mass distributions of neutron induced fission in ^{235}U and ^{241}Pu to spontaneous fission of ^{248}Cm and ^{252}Cf. The yields of isotopes towards mass 80 are more than one order of magnitude higher compared to spontaneous fission sources. For other mass regions changing the fissioning system gives access to different complementary fission fragments that may thus facilitate the gating and identification of new, weak γ-ray transitions or reduce the chance of an incorrect assignment of a contaminant transition to a given nucleus. Therefore, neutron-induced fission is a very powerful way to complement and extend existing spontaneous fission data sets. Moreover, prompt γ-spectroscopy with HPGe detectors is an excellent complementary approach to neutron-induced fission data obtained from the fission fragment separator LOHENGRIN at the research reactor of the institut Laue-Lagevin (ILL). LOHENGRIN separates fission fragments from an in-pile target in the ILL reactor by mass and kinetic energy. However, with LOHENGRIN only longer lived isomers ($T_{1/2} > 0.3\,\mu$s) are accessible, limited by the flight time through the separator [9]. A first experiment aiming at observing γ-rays from fission fragments at a neutron beam was presented in [10], where isomers in the 50–500 ns time region were studied at the cold neutron beam facility PF1B. This experiment was essential in showing that fragment spectroscopy close to a neutron beam is feasible.

Table 1. Overview of beam time used for particular experiments during the EXILL campaign. Of the 100 days of beam time only 4 days were devoted due to change of configuration or technical defects. More details on the targets and detector configuration can be found in the according sections of the paper.

Beam Time	**Campaign**	**Target**	**Detector Configuration**
7 days	on/off beam test	$BaCl_2$, ^{152}Eu, ^{60}Co	Config. 1: 8 EXOGAM, 2 ILL, 6 GASP
14 days	(n,γ)	^{48}Ca, ^{77}Se, ^{96}Zr ^{167}Er, ^{194}Pt,	
16 days	(n,f)	^{235}U on Zr backing	
6 days	(n,f)	^{235}U on Be backing	
7 days	(n,γ)	^{96}Zr, ^{155,157}Gd, ^{161}Dy, ^{209}Bi	
10 days	(n,γ) fast timing	^{46}Ca, ^{96}Zr, ^{209}Bi, ^{48}Ti	Config. 2: 8 EXOGAM, 16 FATIMA
13 days	(n,f) fast timing	^{235}U on Be backing	
1 day	(n,γ)	^{195}Pt	
10 days	(n,f) fast timing	^{241}Pu on Be backing	
1 day	(n,γ)	^{95}Mo	Config. 3: 8 EXOGAM only
1 day	(n,γ)	^{143}Nd	Config. 4: 9 EXOGAM, 2 ILL, 5 GASP
14 days	(n,f)	^{241}Pu on Be backing	

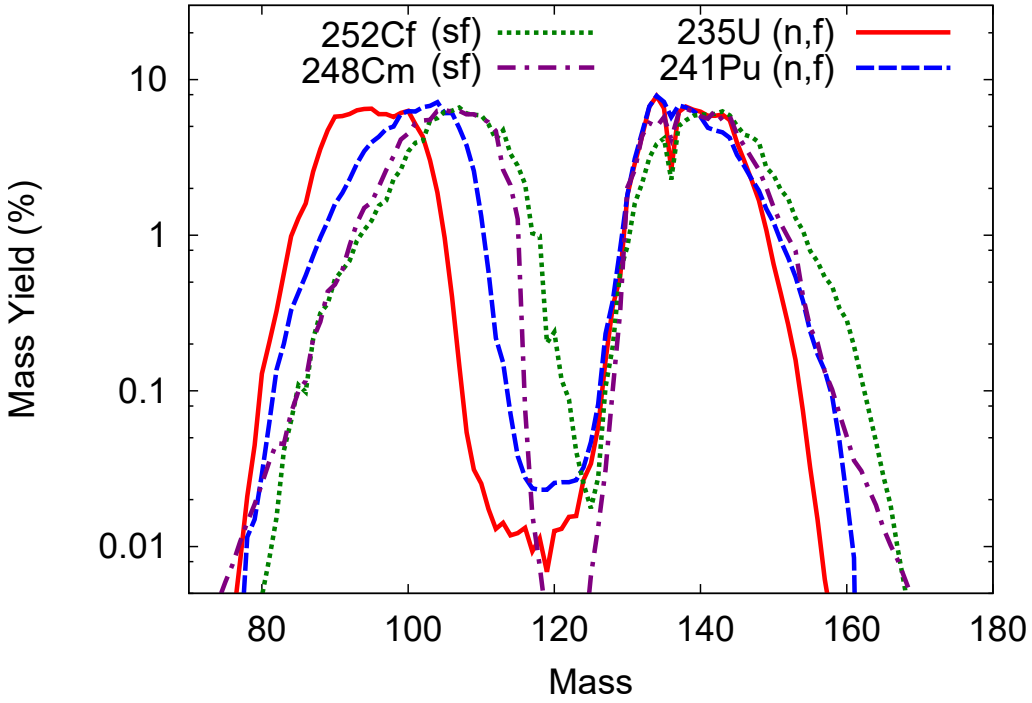

Figure 1. Fission fragment mass distribution following the neutron induced fission of ^{235}U and ^{241}Pu compared to the mass yields of spontaneous fission of ^{248}Cm and ^{252}Cf. The data were extracted from [8]. In the region towards mass 80 the yields are considerably higher in neutron induced fission than in spontaneous fission.

The installation of a HPGe-array at a neutron beam facility can be further motivated by the completeness of the spectroscopy of (n,γ) reactions. Due to the non-selectivity of the capture reaction the majority of the low-spin excitations in a given nucleus are populated giving access to a very rich and detailed spectroscopic information close to the line of stability. Present data sets are often resulting from a combination of data from ultra-high resolution γ-spectroscopy carried out with crystal spectrometers for low-energy transitions ($E_\gamma < 1.5$ MeV) and data from a single HPGe detector for higher energies [11, 12]. Level schemes built from such data sets were made using Ritz-combination algorithms [13, 14], which themselves are not too robust with respect to false placements, if the level scheme is above a certain level of complexity. This has led to cases where several hundreds of measured transitions could not be placed in the level scheme. For many cases a complementary experiment allowing a set of true coincidences would help to remove uncertainties in the level scheme.

A large number of complementary techniques giving access to additional information can also be explored. These include lifetime measurements, based on a fast-timing technique with lanthanum bromide scintillators [15], or Doppler-shift attenuation methods [16], study of nuclear fission dynamics [17, 18], g-factor measurements [19, 20] and many others. All this was driving the idea of bringing a high efficiency HPGe detector array to the intense cold neutron beam facility PF1B at the ILL for a beam time of 100 days (2 reactor cycles). The first reactor cycle was devoted to spectroscopy measurements and the second reactor cycle was shared between fast-timing measurements and γ-ray spectroscopy.

2017 JINST 12 P11003

We will refer to the campaigns as EXILL (**EX**OGAM@**ILL**) and EXILL+FATIMA for the combination with the fast timing array FATIMA. The latter campaign is described in detail in a separate paper [15]. Table 1 gives an overview on the beam time use. The following sections describe in detail the individual components of the experiment. In the final section some reference measurements are shown demonstrating the performance of the set-up.

2 The cold neutron beam facility PF1B and the neutron collimation system

The ILL research reactor supplies a large number of neutron guides allowing for transportation of neutrons from the institute's high flux reactor over tens of meters to experimental areas. The most intense of these neutron beams is provided by the ballistic super mirror guide H113 feeding the cold neutron beam facility PF1B. The experimental zone of PF1B, enclosed in-between casemates of other neutron guides, is equipped with a dedicated shielding to minimize the γ and neutron background of the neighbouring instruments and neutron guides. A detailed description of the characteristics of H113 can be found in [21, 22]. The neutron guide delivers a thermal neutron capture-equivalent flux density of $2.2 \times 10^{10}\,\mathrm{cm}^{-2}\mathrm{s}^{-1}$ at a nominal reactor power of 58.3 MW (the higher flux compared to [22] is due to upgrades and replacement of degraded guide components) on an exit window of $20 \times 6\,\mathrm{cm}^2$. The spectrum-averaged divergence was 7 mrad FWHM [22] before the upgrades and replacements. Such a large beam profile and its divergence are not suitable for γ-spectroscopy. Also angular correlation measurements require a geometrically well defined source. Therefore, a dedicated collimation system was designed shaping the beam to a circular profile with about 1 cm diameter five meters downstream from the end of the H113 guide.

The collimation system (see also [3]) consists of a sequence of circular apertures made from strongly neutron absorbing materials. We chose sintered natural boron carbide (19.9% natural abundance of ^{10}B, ^{10}B(n,α) cross section is 3840 b followed by 94% probability of 0.48 MeV γ-ray emission) and sintered enriched ^{6}LiF (^{6}Li(n,α) cross section is 940 barn, no γ-ray emitted). To suppress the γ-ray background from boron, all according apertures are shielded with 5-cm thick lead absorbers downstream of the neutron beam direction. The sequence of apertures is inserted in a cylindrical vacuum tube system made from aluminum, the inside walls of which are completely covered by 1-cm thick borated plastic. The boron in the plastic serves to absorb the neutrons scattered (and not captured) from the apertures. The tube system consists of 8 segments, which are aligned when assembled together with an uncertainty in the mechanical transversal misalignment not larger than 1 mm over the entire length of the collimation system. All apertures are mounted offline in the individual sections and the system can be fully or partially assembled and then installed in the experimental zone. The first two apertures consist of precision machined 1-cm thick B_4C ceramics, each mounted on a 5-cm thick lead aperture. The following three collimators consist of 5-mm thick ^{6}LiF ceramics mounted on 3-cm thick borated polyethylene, supported by 5 cm thick lead apertures. The holes in the supporting apertures were protected by ^{6}Li loaded rubber sheet against scattered neutrons and were large enough to exclude contact with the direct beam. The total length of the aperture sequence is about 4 m, followed by a 1-m free flight path section containing vacuum pump access. The target chamber of about 1 m length itself is attached (see section 3), which is followed by a 1-m long beam dump pipe, which ends with a 5-mm thick ^{6}LiF ceramics. The vacuum tube leading to the beam dump is lined with 2 cm boron loaded rubber sheet

2017 JINST 12 P11003

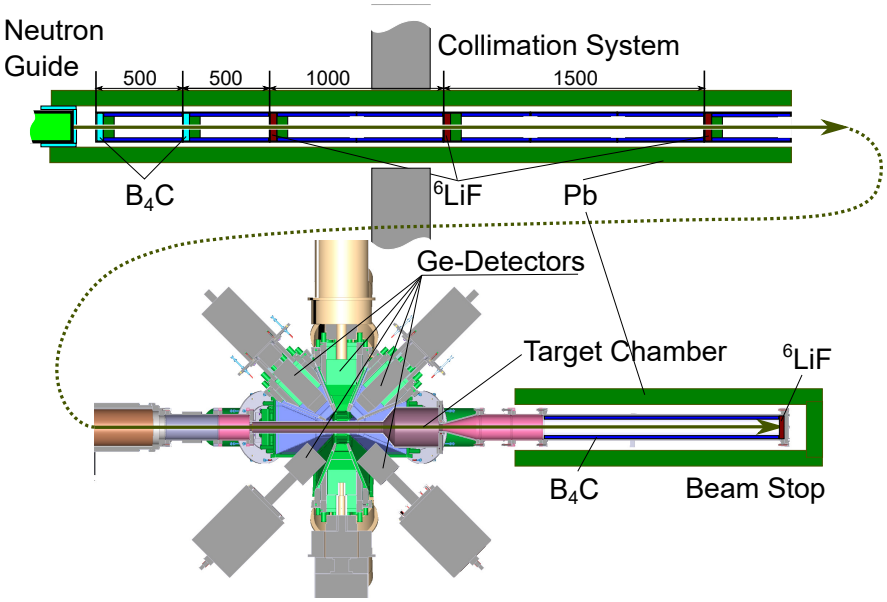

Figure 2. Schematic layout of the collimation system with its sequence of apertures. The collimation system is followed by the target chamber, the detector array and a beam dump.

to absorb neutrons backscattered from the dump in the target section. An illustration of the installed collimation system is shown in figure 2.

The neutron beam position and profile were verified with RTQA2 and EBT2 Gafchromic films. These self-developing dosimetry films are usually employed for quality assurance in radiotherapy applications. The active layer consists of lithium pentacosa-10,12-diynoate (LiPCDA), a diacetylene monomer containing also lithium and nitrogen. Slow neutrons captured on these elements emit short-range charged particles via the ^{6}Li(n,α) and ^{14}N(n,p) reactions which induce local polymerization and consequently a blackening of the film. Exposure to neutron fluences above $10^{10}\,\mathrm{cm}^{-2}$ leaves a clearly visible beam spot on the film, see figure 3. The irradiation time was chosen such that the optical density as function of neutron fluence was changing linearly with good approximation. This allowed the neutron fluence distribution to be derived from the measured optical density distribution. The films were scanned using commercial office scanners and digitized.

The collimation system at the H113 neutron guide was simulated using the McSTAS [23, 24] simulation package for neutron transport. The simulation models neutron propagation from ILL's vertical cold source along the H113 guide (according to [21] and taking into account all upgrades), through the collimation system until the beam stop. A comparison of simulated and measured beam profile in the target position is shown in figure 3. It is worth mentioning that this beam profile has been measured about 1.3 m downstream of the last collimation aperture. The FWHM of the measured profile is about 12 mm and in good agreement with the simulations, demonstrating the good alignment of the collimation system. The divergence of neutrons at the guide exit is wavelength dependent. It can be seen (figure 3) that longer wavelengths are suppressed more strongly than short ones. The average wavelength determined from the simulated capture equivalent spectrum of the neutron beam at the target position is $\lambda_n = 4.6(2)$ Å, corresponding to $E_{\mathrm{kin}} = 3.9(4)$ meV, where the error is dominated by uncertainties in modeling the ILL reactor's vertical cold source.

2017 JINST 12 P11003

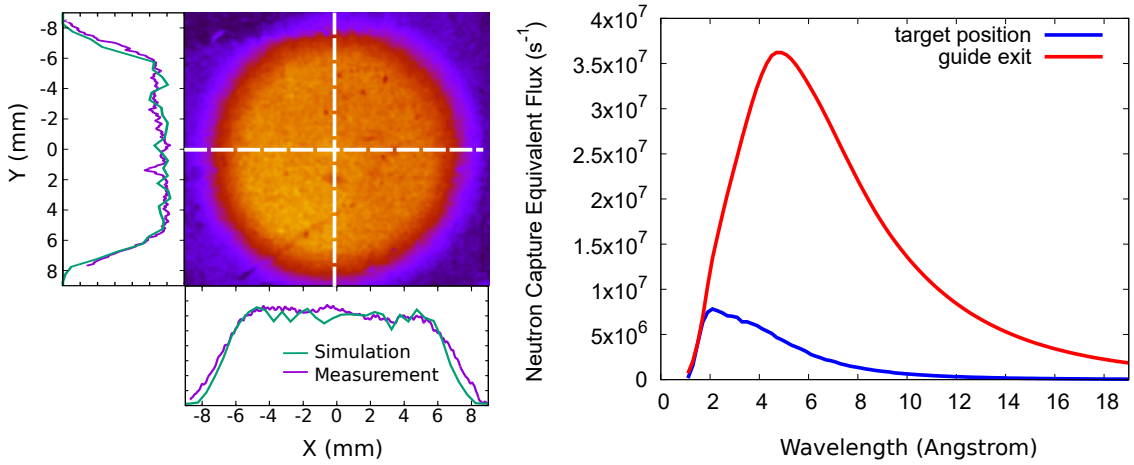

Figure 3. Left hand side: measured beam spot at the target position, 1.3 meters downstream of the last collimation aperture. The graphs show cuts of the 3D profile comparing them to Monte Carlo Simulations using the neutron transport code McSTAS [23, 24]. Right hand side: simulated neutron capture equivalent spectrum at the guide exit and the target position. The difference in shape is caused by the stronger suppression of longer wavelengths due to their larger divergence at the guide exit.

3 The target chamber

The design of the target chamber had to fulfill several requirements. On one hand it was necessary to provide optimal conditions for γ-ray spectroscopy. This demands a minimum amount of material absorbing or scattering γ-rays emitted from the target, a low production of γ-background by neutrons scattered by the target, a close positioning of the detectors around the target position and the possibility to easily change the target. On the other hand the target chamber should allow highly radio-toxic targets to be used such as ^{241}Pu. These targets have to be loaded and unloaded in ILL's dedicated alpha activity laboratory. Furthermore a double wall containment of these targets together with certain other safety requirements with respect to tightness, mechanical robustness as well as leakage monitoring was necessary.

These complex requirements have led to the design of a double-wall target chamber system, which can be operated in two configurations. A first configuration uses only the outer shell of the target chamber. This configuration is fully optimized for (n,γ) and ^{235}U(n,f) experiments as low radio-toxic targets. The target chamber is made of an aluminum pipe of 50 mm diameter with 2 mm wall thickness. It is directly connected to the collimation and beam stop vacuum system. Samples were inserted and held in teflon bags fixed via teflon wires to a small metal frame. The metal frame was inserted and reproducibly plugged into position by opening the connection flange between target chamber and beam stop tube. If an enhanced security configuration is required, a second inner target chamber is inserted instead of the target holder frame. This second chamber is made of an aluminum tube of 35 mm inner diameter and 2 mm wall thickness. It was loaded, sealed and vacuum pumped in ILL's alpha activity laboratory. The neutron beam enters and exits via 200-μm thick zirconium windows to minimize neutron scattering. The collimation system, the outer vacuum chamber and the beam stop tube were filled with helium gas, at a pressure of 50 mbar, and the inner chamber was equipped with a vacuum gauge allowing the chamber integrity to be

2017 JINST 12 P11003

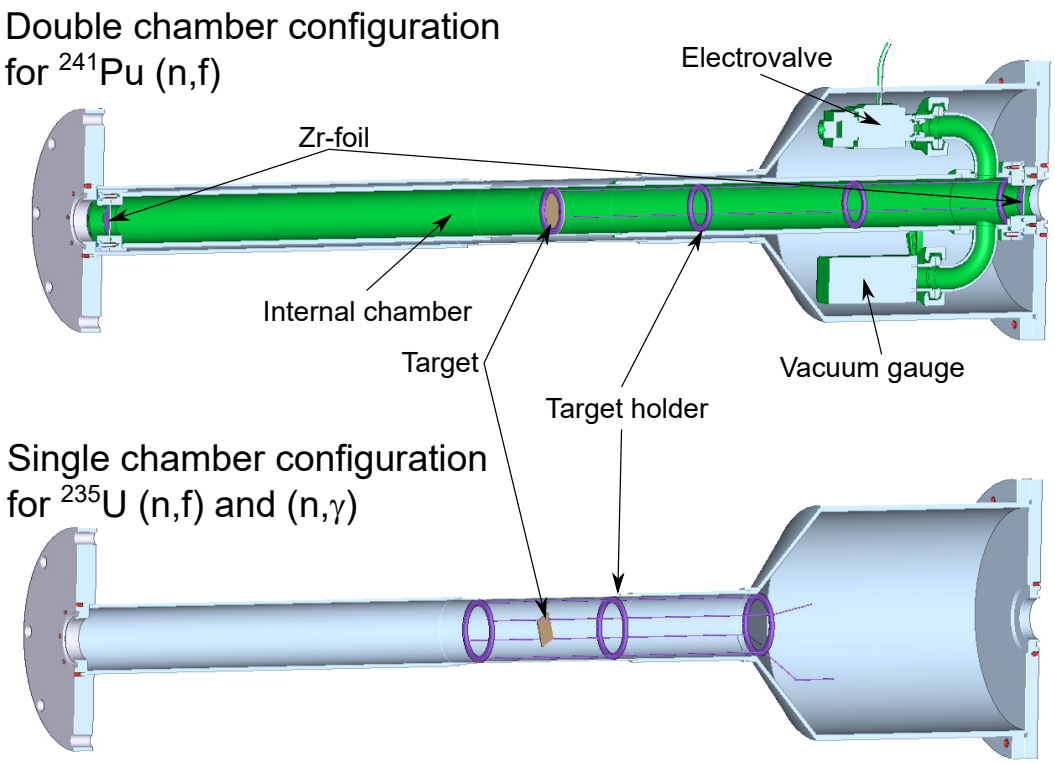

Figure 4. Schematic view of the double wall target chamber: in the lower part the target chamber system is shown as it was used in single wall configuration for (n,γ) and ^{235}U(n,f) experiments. The target holder frame is drawn in purple, the target teflon bag in beige. The upper part of the figure shows the double wall configuration. The second (internal) chamber is shown in green. It is a completely independent chamber, which is inserted into the outer chamber. Samples are loaded into the inner chamber in ILL's alpha activity laboratory and the chamber is vacuum pumped and sealed. The inner chamber is equipped with a vacuum gauge allowing to monitor its tightness during operation.

monitored during the experiment. A schematic view of the target chamber system is shown in figure 4. In both configurations, the outer target chamber was surrounded with a 1 mm thick ^{6}LiF rubber sheet in order to absorb any remaining scattered neutrons.

The impact of the different components of the target chamber on the background was optimized. This is illustrated in figure 5. The first spectrum compares the impact of the outer single wall chamber and empty target holder with open beam to ambient background (closed beam). It can be seen that the contributions from the target environment are very small. The γ-rays from a 3.2 mg $BaCl_2$ target appear with two orders of magnitude more intensity. However, by analyzing the spectrum, the presence of γ-rays of Ge and Al pointed to a substantial scattering of neutrons from the target to the outside. This was suppressed by adding the mentioned ^{6}LiF-rubber sheet around the target chamber. In the same way the effect of components of the second, inner target chamber was optimized. The right-hand side of figure 5 illustrates the impact of the Zr-window on the exit of the inner chamber. It adds substantial background by scattering neutrons into the Ge-detectors. This was suppressed by adding ^{6}LiF around the exit of the inner chamber. Furthermore, the figure illustrates the impact of the Zr backing for the first ^{235}U target.

2017 JINST 12 P11003

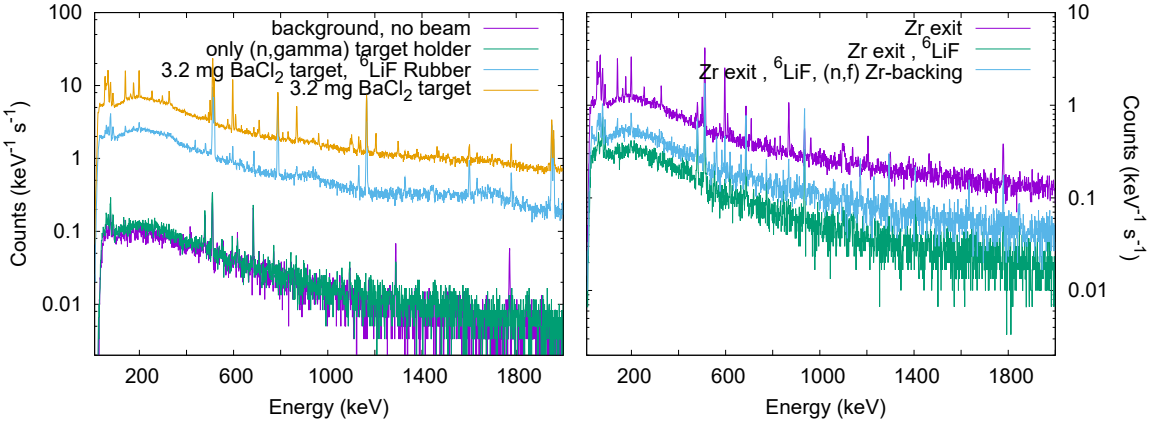

Figure 5. Left hand side: comparison of background in the (n,γ) configuration induced by single chamber and empty target holder to ambient background of the PF1B experimental zone. Furthermore, the spectrum from a 3.2-mg $BaCl_2$ target is shown. Neutron scattering by the target generates additional background, which was suppressed by ^{6}LiF-rubber sheet around the target chamber. Right hand side: impact of a Zr-window and a blank Zr target backing from the inner target chamber for the first ^{235}U target. The impact of the Zr-window was minimized by additional ^{6}LiF enclosing of the exit window.

4 Targets

The neutron-capture cross section of the target isotopes studied in the EXILL campaign covered a wide range from 2.3×10^{-2} to 2.54×10^5 barns. This required careful target preparation, which is described in the following sections. In particular the target mass should be choosen so as to assure a reasonable count rate of the detectors and an acceptable level of attenuation of low-energy γ-rays in the target. The chemical compounds of the targets were selected to minimize elastic scattering of neutrons.

4.1 Stable targets

Table 2 summarizes the properties and irradiation times of all targets. All stable targets were conditioned in individual FEP (fluorinated ethylene propylene copolymer) bags. These bags were made from thermosealed 25-μm thin FEP foils (Goodfellow FP341025). The actual target mass was determined by weighing empty and filled bags, respectively. The FEP bags containing the samples were mounted perpendicularly to the neutron beam, held in place by thin PTFE (polytetrafluoroethylene) strings (Goodfellow FP345925). The ^{46}Ca target was made by drying a ^{46}Ca-nitrate solution directly in a double teflon bag to avoid any loss of the precious material. The ^{155}Gd and ^{157}Gd targets were both made from a single tiny grain of Gd_2O_3 powder enriched in ^{155}Gd and ^{157}Gd, respectively. The grain was fixed with glue and wrapped into a bag of 10-μm thick aluminum foil and the FEP bag to prevent accidental spreading in the vacuum chamber. Due to the enormous neutron-capture cross-sections of ^{155,157}Gd these samples act as a "black" absorber for neutrons. Hence, the (unknown) grain area perpendicular to the beam instead of the grain weight determines the capture rate. The latter was adjusted to match the count rate capability of the detector array by attenuating the neutron flux in-between neutron guide and entry of the collimation system, i.e. 5 m upstream of the target. This was achieved by inserting a 5 mm thick plexiglas sheet as scatterer in

2017 JINST 12 P11003

Table 2. Overview on the majority of used (n,γ) targets during the EXILL campaign. Fission targets are separately described in the text. Column (A:B) refers to isotope of interest:chemical compound, (C) to physical form, (D) to isotopic enrichment, (E) to percentage of neutron captures in the isotope of interest relative to all captures in the target, (F) to fraction of scattered neutrons, (M) to total count rate, (N) to the target mass, (O) to the amount of substance of the isotope of interest multiplied by its neutron capture cross section, (P) to the total irradiation time and (Q) to publication.

A:B	C	D (%)	E (%)	F (%)	M (kHz)	N (mg)	O (mmol× barn)	P (h)	Q
^{35}Cl:$BaCl_2$	powder	75.8			70	9.6	2.51	1	
^{46}Ca:$Ca(NO_3)_2$	chunk	31.7	32	0.3	82	40.6	0.12	70	
^{48}Ca:$CaCO_3$	powder	69.2	48	1.7	220	354	3.01	65	[25]
^{48}Ti:Ti	foil	73.8	95	0.8	540	84	7.58	13	
^{68}Zn:ZnO	powder	99.2	96	1.0	160	250	3.36	23	[26]
^{70}Zn:ZnO	powder	98.8	86	0.9	540	250	0.32	20	[26]
^{77}Se:Se	powder	99.7	99.7	< 0.1	220	6.0	3.27	21	[27]
^{96}Zr:ZrO_2	powder	59.6	14	2.0	470	700	0.55	14	
^{95}Mo:Mo	disk	96.5	99.8	0.1	170	16.9	2.25	41	[28]
^{143}Nd:Nd	metal	91.1	> 99.5	< 0.1	200	0.8	1.72	36	
^{155}Gd:Gd_2O_3	grain	93.1	88.6	< 0.1	313	< 1		16	[29]
^{157}Gd:Gd_2O_3	grain	94.4	99.4	< 0.1	390	< 1		17	
^{161}Dy:Dy_2O_3	powder	91.7	90	0.2	500	1.7	5.15	55	
^{167}Er:Er_2O_3	powder	91.5	99.9	< 0.1	230	1.1	3.48	19	
^{194}Pt:Pt	foil	96.5	66	0.9	230	202	2.18	19	[30]
^{194}Pt:Pt	2 balls +powder	96.4	63	0.8	180	192	2.16	11	
^{194}Pt:Pt	foil +powder +2 balls	96.4	64.8	1.7	230	393	4.34	42	
^{195}Pt:Pt	foil	33.8	90	0.5	620	143	7.56	16	[31]
^{209}Bi:Bi	2 disks	100	100	1.8	83	700	0.11	4	[32, 33]
^{209}Bi:Bi	balls	100	100	7.9	170	3000	0.49	18	
^{209}Bi:Bi	cylinder	100	100	5.2	100	1960	0.32	47	

front of the neutron beam collimation system. Note that the average capture wavelength (energy) given in section 2 does not apply in these two cases, due to the spectrum change by the plexiglas as well as due to the large cross section of the targets.

4.2 Radioactive targets

Targets of ^{235}U and ^{241}Pu were used for γ-spectroscopy of prompt fission product. Fission products with an recoil energy in the range from 50 to 110 MeV need to be rapidly stopped in order to minimize Doppler broadening of the emitted γ-rays. Thus, the targets were sandwiched between appropriate

2017 JINST 12 P11003

"stoppers" with a thickness sufficient to stop fission products traversing them perpendicularly. The stopper material should have a low neutron-capture cross section, and appropriate physical and chemical properties for preparation in a glove box and use in vacuum. High Z materials are less suitable due to the important attenuation of low-energy γ-rays in the radial direction (where the EXOGAM octagon is located, see section 5).

The ^{235}U material had an enrichment of 99.7% with the remainder consisting of non-fissile uranium isotopes ^{234}U, ^{236}U and ^{238}U. With cold neutrons the total fission rate is completely dominated by the ^{235}U(n,f) reaction. Therefore, considering an average prompt neutron multiplicity of $\nu_p = 2.42$, the average N/Z ratio of fission fragment pairs is 1.539 and 2.539 for A/Z.

One of the ^{235}U targets was made by depositing $^{235}UO_2$ layers by the multiple painting technique [41] on 2-μm thin Zr foils (Goodfellow Zr000080). These were then sandwiched between two 15-μm thick nuclear-grade Zr foils (Advent Research Materials Zr2449). To assure a tight packing the sandwiches were cold-rolled with a few mg/cm^2 metallic tin as filling material. Fission products have nearly identical stopping power in uranium oxide, tin and zirconium. Thus, the sandwich can be considered as a homogeneous stopper. In total a sandwich consisting of 3 layers of $^{235}UO_2$, each sandwiched between Sn and Zr, was mounted. The total ^{235}U mass determined by γ-ray spectrometry was 525 μg. Another ^{235}U target was made by depositing a $^{235}UO_2$ layer by the multiple painting technique on a thick graphite sheet. Subsequently the top graphite layer carrying the $^{235}UO_2$ layer was removed with a scalpel and transferred on a 25.4 μm thick beryllium foil (ESPI Metals, 2N8 purity). A second 25.4 μm thick Be foil was glued on top with superglue (polyacrylate). The total ^{235}U mass of the second target determined by γ-ray spectrometry was 675 μg. Prior to the target preparation, samples of the zirconium foil, tin and superglue had been deposited in a teflon bag irradiated by the neutron beam for a background measurement in the neutron beam. No unexpected neutron capturing impurities had been detected. At present a number of different physics cases based on data from the ^{235}U campaign are already published [15, 34–40].

The ^{241}Pu target was prepared by recycling an old ^{241}Pu target that was previously used in a fission experiment at ILL. The old target was not directly usable for the EXILL campaign due to the high gamma activity of ^{241}Am that had grown in. Moreover the target had a protective gold layer produced by physical vapour deposition which would create considerable (n,γ) background when exposed to neutrons. Hence, at the Nuclear Chemistry Institute of Mainz University the Pu material was chemically purified in several steps and deposited (in oxide form) by Molecular Plating [42] from isopropanolic solution onto a thin Be-foil (25.4 μm, ESPI Metals, 2N8 purity)) as backing. The target spot had a diameter of 8 mm. After drying, a second 25.4 μm thick Be foil was glued with superglue on top. Before and after electroplating, aliquots (20 μl) of the isopropanolic solution were taken and evaporated to dryness onto a little Ta-disc to prepare samples for α-spectrometry. From the activity of the ^{241}Am daughter in both test samples the deposited ^{241}Pu amount was determined to 300(30) μg.

The ^{241}Pu was enriched to 78 % with the remainder mainly consisting of non-fissile plutonium isotopes ^{240}Pu 5 % and ^{242}Pu 16 %. Fissile ^{239}Pu represented 0.02 %. At the beginning of the FATIMA measurement ^{241}Am represented 0.2 % of the target mass (10 kBq), rising to 0.5% (23 kBq) at the end of the measurement period. With cold neutrons the total fission rate is completely dominated by 99.8% from ^{241}Pu(n,f), i.e. considering the average prompt neutron multiplicity of $\nu_p = 2.929$ the average N/Z ratio of fission fragment pairs is 1.543, i.e. slightly higher than that of ^{235}U.

2017 JINST 12 P11003

For all fission targets a γ-ray spectroscopy analysis of the fission product inventory was performed after the experiment. Thus the average fission rate could be deduced from the long-lived fission product activities. For the ^{235}U and ^{241}Pu targets on a Be backing the observed activities of the volatile fission products ^{133}Xe and ^{131}I are consistent with the activities of the non-volatile fission products. This proves that the backing and cover were gas-tight, i.e. no significant fraction of the fission products could escape.

5 Detectors

Within the EXILL campaign for the first time a large HPGe array (up to 49 germanium crystals) has been installed around a target irradiated by a highly collimated cold-neutron beam with a capture equivalent flux of 10^8 cm^{-2} s^{-1} at the target position. Three different-type Ge detectors were used to construct the EXILL detector array:

- Up to 10 EXOGAM Clover detectors [43–45] from the laboratory of the Grand Accelerateur National des Iones Lourdes (GANIL), each consisting of four segmented closed-ended coaxial n-type Ge crystals with a diameter of 60 mm (before shaping) and 90 mm in length. The front side of the Clovers is tapered at a length of about 30 mm. The relative efficiency of each Clover crystal is about 38% and the combined efficiency of one Clover in add-back mode about 220%. Although these detectors are segmented, only the core signal of each crystal was read out.

- Six GASP detectors [46, 47] from the Legnaro National Laboratory (LNL), large volume HPGe detectors made of closed-ended coaxial n-type Ge crystals with a diameter of 70 mm and a length of 80 mm. The front side of the Ge crystals is tapered at a length of about 30 mm. The relative efficiency of the detectors is about 80%.

- Two Clover detectors from the ILL instrument LOHENGRIN consisting of four non tapered closed-ended coaxial n-type crystals with 50 mm diameter (before shaping) and 80 mm length. These Clovers have a 1.5 mm thin Al entrance window to be more efficient for the detection of low-energy γ-rays. The relative efficiency of each Clover crystal is about 25% and the combined efficiency of one Clover in add-back mode about 150% [48].

All detectors were mounted on a dedicated mechanical structure originally designed at GANIL for 16 EXOGAM Clover detectors and adapted to the spatial requirements of the PF1B cold neutron beam facility. In order to cover a large range of physics, four different detector array configurations were realized during the beam time. All of them used an arrangement of 8 EXOGAM Clover detectors into a regular octagon perpendicular to the beam axis as a basis. The remaining detectors were mounted on two half spheres on each side of the ring:

- Configuration 1 used additionally to the EXOGAM octagon the 2 LOHENGRIN Clover detectors and 6 GASP detectors. On the left side of figure 6 the detector placement in the PF1B zone around the target chamber is shown. The two LOHENGRIN Clovers were placed at 45° with respect to the beam axis below the sample, parallel to the beam axis and the GASP detectors were filling the 6 remaining positions at 45°. This configuration was used during the entire first reactor cycle.

2017 JINST 12 P11003

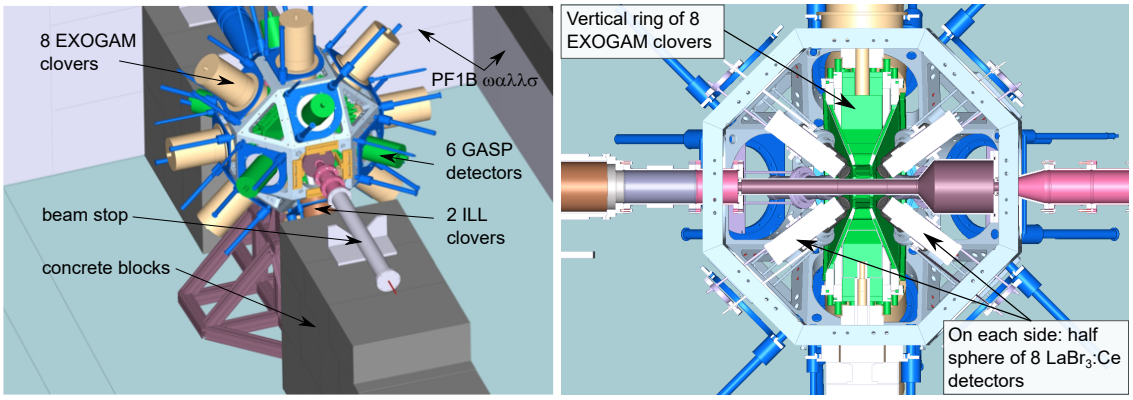

Figure 6. Left side: schematic view of the EXILL setup at the PF1B experimental area. The detector configuration 1 shown here was used during the entire first reactor cycle. In the similar configuration 4 (not displayed here) one GASP detector above the beam axis was replaced by one EXOGAM Clover detector. This configuration was used during the second half of the second reactor cycle. Right side: schematic side view (perpendicular to the beam axis) of the EXILL+FATIMA detector configuration 2. The inner chamber used for the ^{241}Pu(n,f) run is also drawn.

- Configuration 2: the GASP and LOHENGRIN Clover detectors were removed and 16 $LaBr_3$:(Ce) scintillator detectors from the FATIMA collaboration added (see figure 6 right side). A detailed description of this setup is given in reference [15]. These fast response scintillation detectors have an energy resolution of about 3% at 1.3 MeV and an excellent time response (< 200 ps). They are particularly suited for lifetime measurements in the range of a few picoseconds to several nanoseconds. All crystals were 1.5″ in diameter, half of them being 2″ long and the other half being 1.5″ long. They were all mounted on modified Hamamatsu R9779 photomultiplier tubes. This configuration was used during the first half of the second reactor cycle.

- Configuration 3 consisted of the central octagon with EXOGAM detectors only. It was used for two days only during the changeover period to configuration 4.

- Configuration 4 was a high Ge efficiency configuration used during the second part of the second cycle. This configuration was similar to configuration 1 but replacing one GASP by an additional EXOGAM detector (at 45° to the beam above the beam axis).

All the germanium detectors, with the exception of the two LOHENGRIN Clovers (since they are not tapered and thus not geometrically compatible), were equipped with the active BGO (bismuth germanate) Compton-suppression shields of the EXOGAM array. The signals of the individual segments of a BGO detector surrounding one germanium detector were daisy-chained together and recorded with those from the germanium crystals in list mode. Anti-coincidence discrimination was performed off-line. In addition, tungsten collimators were placed in front of the BGO detectors to avoid direct hits in the BGO by gammas from the target and reduce cross-talk between adjacent detectors.

A dedicated automatic liquid nitrogen filling system was developed for the EXILL campaign. Two dewars were used to automatically fill up to 16 detectors three times per day. Moreover,

2017 JINST 12 P11003

all the internal temperature sensors were read allowing automatic emergency filling. When the configuration 4 was adopted, around 200 liters of liquid nitrogen were used per day.

6 The digital data acquisition system

Depending on the detector configuration, the data acquisition system handled up to 72 channels. The analog signals from the detector preamplifiers were sampled by ten V1724 CAEN digitizers [49], which are 1-unit wide VME 6U modules housing eight channels of 14 bit 100 MS/s flash ADC with threshold auto-trigger capabilities. The numerical information about the amplitude of the analog signals and their arrival time were collected by two RIO3 PowerPC-based VME single board computer [50] (data concentrator) before being recorded on a computer hard disk. The total event rate achieved was about 900 kHz events corresponding to a data rate of 7.2 MByte/s. In order to properly propagate the timing information across several ADCs, the internal clock of each digitizer board was phase locked to an external clock source provided by a single V1724 module defined as master clock board. Each digitizer consists of a common motherboard housing specific mezzanine cards for each channel. The motherboard hosts the clock logic management and the readout control FPGA that provides the trigger management and acts as a bridge between the local bus and the different interfaces (VME 64X as used with EXILL, Optical link, PCI express, USB 2.0). Mezzanine cards house the analog input front-ends and the channel FPGA that accounts for the analog-to-digital conversion, the digital pulse processing algorithm and the memory buffers. The readout controls the FPGA accesses of the mezzanine cards through the local bus.

A specific Digital Pulse Processing (DPP) algorithm implemented in the FPGA of the digitizers allows to extract the amplitude and the arrival time of the detected pulses. Pulse conversion starts with a trigger generated by a voltage step exceeding a programmable digital threshold. For an accurate time determination the FPGA calculates the second derivative of the input signal (the direct output of the detector preamplifier). Since the input signal can be represented as the sum of two exponential decays, with the fast component determined by the charge collection time of the detector and the slow one by the RC of the preamplifier, it can be shown that the zero crossing of such a second derivative depends only on the two time constants while it does not depend on the pulse amplitude. Therefore, the zero crossing of the second derivative of the input signal delivers a time determination with an uncertainty equivalent to one unit of the sampling time (10 ns).

At the same time, a trapezoidal filter is applied to the input signal to transform the typical exponential decay generated by a charge sensitive preamplifier into a trapezoid [51]. The height difference between the signal baseline and the flat top of the trapezoid is proportional to the amplitude of the initial pulse. Figure 7 shows all the relevant parameters necessary for a proper determination of the pulse height. This trapezoid plays the same role as the shaping amplifier in a traditional analog acquisition system. Both systems have a shaping time constant that must be properly calibrated for the pole-zero cancellation. Moreover, for both systems a long shaping time gives a better energy resolution but increases the probability of pile-up.

The real-time acquisition engine is implemented in a Power PC based VME board computer equipped with 256 MB of memory. This board does not contain any operating system in order to optimize real-time performances and to minimize any dead time. A specific set of routines has been developed to implement all the functionalities necessary to configure and access the digitizers.

2017 JINST 12 P11003

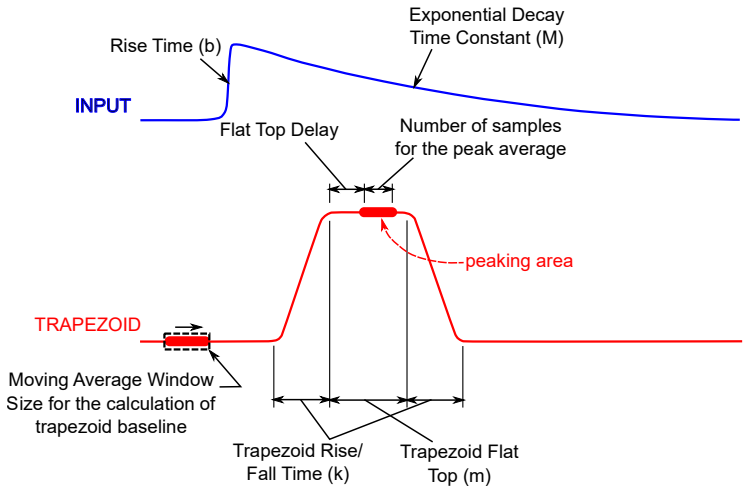

Figure 7. Schematic view of the trapezoidal filter with the relevant parameters.

The real-time processing algorithm running in the processor is able to handle total event rates of more than 1 MHz, providing on-line display for singles and coincidence events of multiplicity 2. The primary purposes of the data concentrator card is to create the data structures containing the variables and the parameters for the acquisition. Once the digitizers have been initialized and programmed, the concentrator is reading the data by emptying the digitizers buffers using MBLT transfer mode over the VME bus. Each event is then on one hand analyzed to produce the relevant online histograms and, on the other hand, stored in a double buffer memory once all the information necessary to define a list-mode event has been added.

ILL in-house instrument control software is then reading asynchronously the cards memory, via a PCI optical link, to transfer the list-mode events to the external mass storage and to display the histograms. In addition the software offers a full graphical interface to access all parameters related to the configuration of the digitizers as well as of the acquisition card. It provides real-time visualization of all relevant spectra including single and multiplicity 2 events, as well as count-rates for higher multiplicities (up to multiplicity 8) and efficiency of Compton suppression. The software includes an oscilloscope mode display, used during the setup phase, to tune the sampling parameters for each channel of the digitizer cards. This mode offers the unique advantage to visualize instantaneously the effects of any parameter modification with respect to all signals involved in the acquisition.

During the fast timing campaign with configuration 2 the digital acquisition system was completed by an analogue "fast-timing" electronic circuit, which is described in more detail in [15] and references therein.

7 Key performances

The data taking was subdivided into short runs to produce files of about 2 Gbyte in size. Since the target quantity was chosen to yield a count rate of about 10–20 kHz per channel, each experiment was subdivided into time intervals of the order of 7–15 minutes, while each run had enough statistics to monitor the systems performances. In-between individual campaigns or changes of

2017 JINST 12 P11003

setup calibration runs with sources of ^{133}Ba, ^{60}Co and ^{152}Eu for lower energies and ^{35}Cl(n,γ)^{36}Cl measurements for higher energies were carried out. During campaigns with open neutron beam, (n,γ) lines from the target backing and chamber material were also used for energy calibration monitoring.

During the whole EXILL campaign, about 60 TB of data have been recorded. The data are available to the EXILL-collaboration via an irods server for download [52]. For this purpose resources from CCN2P3[1] and LPSC[2] were used to store the raw data through the irods protocol. Such irods facility permits to establish access modes with password protection for specific sub-data sets. Accordingly user groups can be granded access to data relevant for their particular measurement campaign only, while the remaining data stay protected. Due to a high degree of parallelisation on the server side a fast access to the data is achieved. This allows remote data evaluation without the need of large data transfer.

7.1 Alignments and calibrations

7.1.1 Energy alignments and calibrations

Figure 8 compares the calibration spectra of the detector system obtained with a 420 kBq ^{152}Eu source after the first ^{235}U campaign (^{235}U on Zr backing) and 12 days later at the end of the first reactor cycle. The FWHM resolution of the system calculated at 1408 keV using both, standard gain matching and drift monitoring routines, is rather stable at around 3.7 keV. (More advanced algorithms based on a splitting the data into low and high energy and therefore obtaining energy depending non-linear terms of the calibration achieve a resolution of 3.2 keV at 1408 keV). To illustrate time dependence we used the same calibration parameters for both data sets resulting in a peak shift of about 200 eV for the 1408 keV peak. While in the raw data at low γ-energies these variations were still small, at high energies these shifts often exceeded the peak width. The left-hand side of figure 9 shows an example of such a variation for one of the Ge detectors at the 7724 keV γ-line from a parasitic ^{27}Al(n,γ) capture reaction accompanying the ^{235}U(n,f) measurement. The pronounced time signature is due to liquid nitrogen filling of the detectors and the consequent local temperature variation.

For the periodical energy calibration monitoring of the EXILL array γ-lines in the range 0–8 MeV listed in table 3 were selected, which have energies known with an accuracy of at least 0.02 keV. The gain matching has been performed for each run to compensate for variations due to external conditions. An automatized procedure was developed to perform the alignment run by run (for the ^{235}U(n,f) measurement about 3500 runs were recorded). The resulting final energy calibration was 0.95 keV per channel with zero offset. After the gain matching, the add-back procedure and the sorting of the data into a histogram a final precise energy calibration was necessary. In the case of the ^{235}U(n, f) measurement we selected 30 known γ-lines observed in all the measurements. It was possible to fit a single, second-order polynomial function to all the points with very good accuracy. The deviation of experimental points from the fitted curve are shown in the right-hand side of figure 9.

[1]Centre de Calcul del Institut National de Physique Nucleaire et de Physique des Particules.
[2]Laboratoire de Physique Subatomique et Cosmologie.

2017 JINST 12 P11003

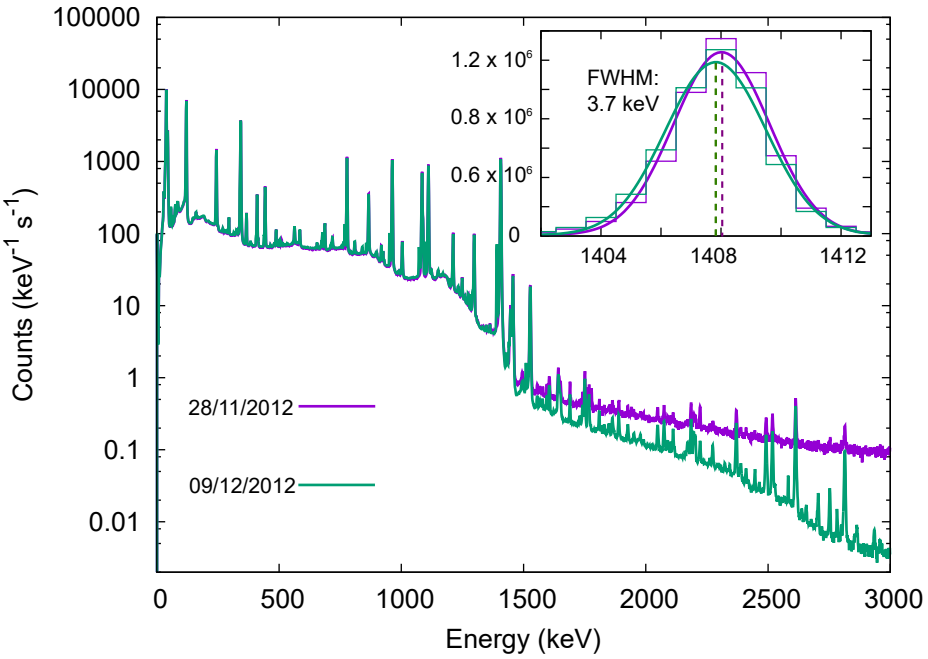

Figure 8. Comparison of two calibration spectra with a ^{152}Eu source. The resolution of the combined detector array at 1408 keV was of the order of 3.7 keV. It can be seen that the energy calibration was not constant over time. The two spectra differ for higher energies (above 1500 keV) since the measurement of 09/12/2012 was taken during the reactor shut down, during which the prompt neutron capture does not contribute to the ambient background in the experimental zone.

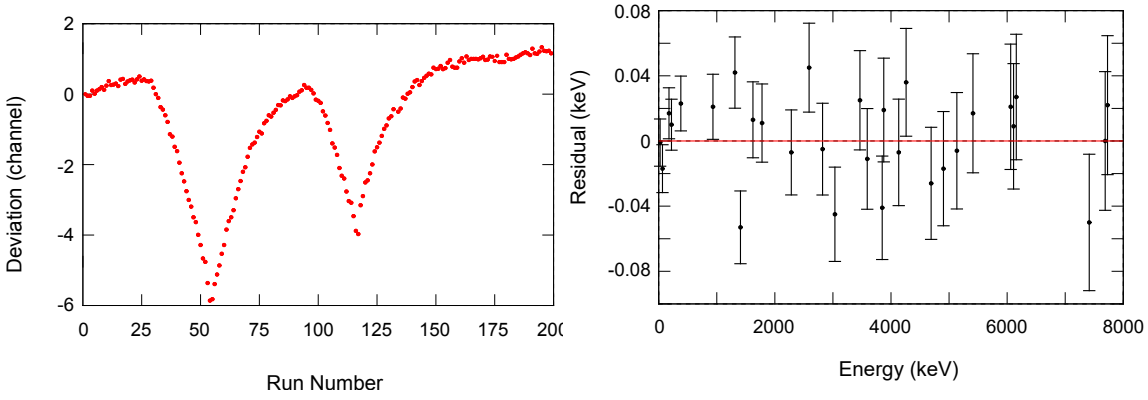

Figure 9. Left hand side: drift of the peak position of the 7724 keV γ-line from the ^{27}Al(n,γ) capture reaction as a function of run number over 24 h. The pronounced signature is due to detector filling and consequent temperature variations. Right hand side: accuracy of the final energy calibration of the EXILL detector array for the ^{235}U-campaign. The data points show the residuals for 30 known γ-lines with respect to the calibration fit.

2017 JINST 12 P11003

Table 3. List of γ-ray transitions used for calibration monitoring and automatic gain monitoring.

Energy (keV)	Error (keV)	Energy (keV)	Error (keV)
58.86	0.02	61.21	0.02
296.44	0.02	312.59	0.02
510.99	0.02	539.65	0.03
1778.92	0.02	1881.31	0.02
2223.25	0.02	2351.50	0.03
3033.90	0.01	3209.24	0.02
3465.06	0.01	3665.52	0.07
4259.53	0.01	4506.35	0.12
4690.68	0.01	4962.57	0.12
5134.34	0.01	5432.06	0.15
7213.04	0.01	7631.98	0.05
7724.03	0.01	8172.76	0.04

7.1.2 Efficiency calibration

The relative full-energy-peak efficiency calibration has been performed using γ-transitions from calibration sources (^{152}Eu and ^{133}Ba), the ^{35}Cl(n,γ) reaction and following ^{235}U(n,f) (from prompt-γ, yrast cascades and β decay of fission fragments). Data points (γ-energy and relative efficiency) that were taken into account are presented in figure 10.

The efficiency of the low-energy region was determined by using γ-transitions coming from the β decay of fission products and the ^{133}Ba calibration source. It is important to emphasize the remarkably high efficiency at low energy. This unique performance could be achieved because of the digital signal treatment, allowing to efficiently apply lower trigger settings for the individual channels. The efficiency values for the middle-energy γ-lines were, predominantly, based on the calibration source ^{152}Eu. The comparison between values obtained from $\gamma\gamma$-gated and γ-singles spectra was made yielding consistent results. Efficiencies for γ-transitions coming from fission products are also in agreement within uncertainty with the ones from calibration sources. The high-energy section was fitted using data points from the (n, γ) reaction on ^{35}Cl. One should note that the efficiency of the system drops quickly above 3 MeV. The drop is coming from the saturation of the preamplifiers of the GASP detectors and the pair production effect. To the data points shown in figure 10 the following 5-parameters function [53, 54] was fitted:

$$\epsilon_\gamma(E) = \exp\left(a_1 - (a_2 + a_3 \exp(-a_4 E)) \exp(-a_5 E) \log \frac{E}{E_0}\right). \tag{7.1}$$

The parameters obtained from a least-squares fit are listed in table 4. The total uncertainty of the efficiency has two components: an error coming from the uncertainties of the fit parameters and the systematic error

$$\Delta_{\text{efficiency}} = \sqrt{\Delta^2_{\text{fit}} + \Delta^2_{\text{systematic}}}. \tag{7.2}$$

The first term in eq. (7.2) is less than 1 % in the middle-energy section (120–5500 keV), it grows at low and high energies, and it is particularly dominating for very low energy. The second term in

2017 JINST 12 P11003

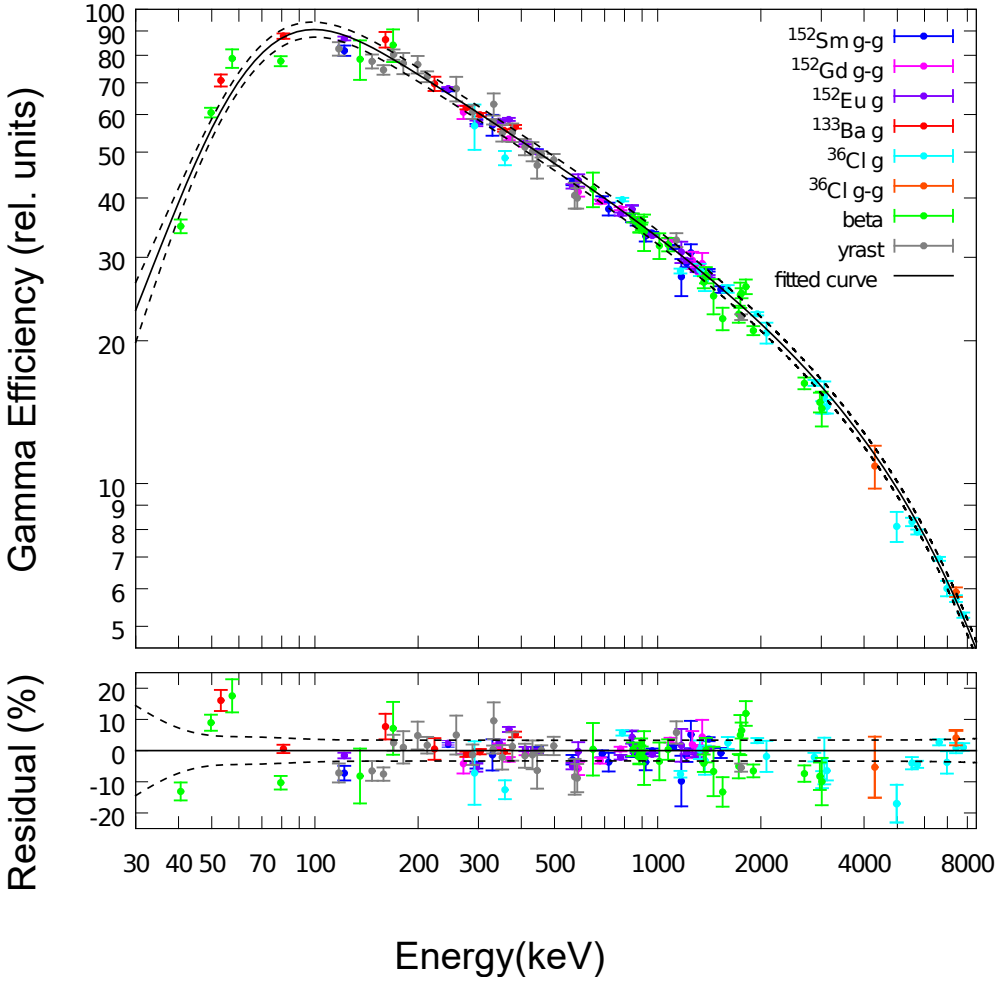

Figure 10. Relative full-energy-peak efficiency (including add-back) for the EXILL set-up. In the top panel, all experimental points are presented, the notation "g" refers to single, the notation "g-g" to γ-rays measured in coincidence. The fitted function (solid line) is drawn together with a "corridor of errors" (dashed lines) corresponding to one standard deviation. In the bottom panel, the fit residual are presented using the same relative units together with the one-standard-deviation "corridor of errors" (dashed lines).

eq. (7.2) is assumed to be a constant fraction of the efficiency predicted by the fitted function. Its value of 3.3 % is obtained after imposing the condition that about 68 % of the data points should be within one uncertainty from the fit.

Table 4. Results of the least-square fit for the parameters of the efficiency function (7.1). The value of E_0 was set to 1 keV.

a_1 = 6.649(36)	a_3 = 2.49(35)	a_5 = -2.96(10)·10^{-5} keV^{-1}
a_2 = 0.4428(58)	a_4 = 4.79(30)·10^{-2} keV^{-1}	E_0 = 1 keV

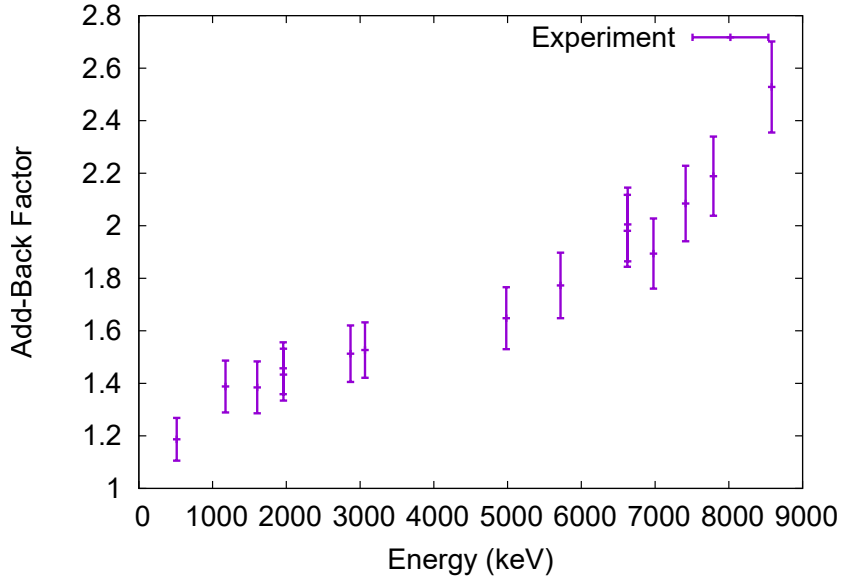

Figure 11. Energy dependence of the Add-Back factor of the EXOGAM clovers determined for energies up to 8 MeV.

The Add-Back factor of the EXOGAM clovers was determined up to the typical neutron binding energies of about 8 MeV and is illustrated in figure 11. The total efficiency of the array in configuration 4 was about 6.5 % at 1.3 MeV.

7.1.3 Time alignments and calibrations

At the beginning of each run the master clock was set to zero, providing a general synchronization of all electronic channels every few minutes. During the runs all digitizer cards are maintained PLL-locked on a 100 MHz reference signal generated by a 1 GHz oscillator on the master board (see section 6). However, due to different detector types, different cables or preamplifiers the detector signals do not arrive simultaneously and an offline time alignment is needed. To do so, we produced time-difference spectra between the time response of a selected (reference) detector and time responses of all other detectors. In the first step one of the Ge detectors was chosen as a reference and time differences to BGO anti-Compton-shield detectors were obtained. The BGO signals, arriving about 300 ns before the Ge signals showed time-misalignments of up to 20 ns, which were then corrected to be less than 10 ns. In the second step, taking any of the time-aligned BGO detectors as a reference detector we produced time-difference spectra for all Ge detectors. The left-hand side of figure 12 shows, on a common time scale, an example of such spectra for pairs BGO-BGO and BGO-Ge detectors. We have aligned all the prompt peaks within 10 ns. Some of the Ge detectors had worse time resolution than others, which has deteriorated the quality of the total time prompt peak. In the right-hand side of figure 12 we show the prompt time peak corresponding to time-differences between all Ge-Ge pairs of detectors, obtained from the full data set of the 16-day measurement of ^{235}U(n,f) in configuration 1. The width of the peak is about 120 ns, approximately twice the width of a prompt peak for a Ge-BGO pair, with a single-Ge crystal gated on a high-energy γ-line (dashed line).

2017 JINST 12 P11003

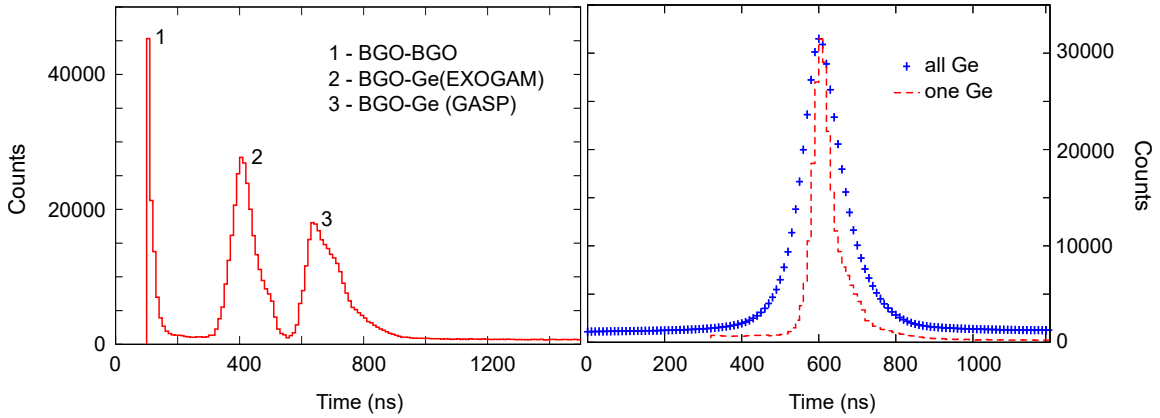

Figure 12. Left hand side: time-difference spectra for pairs BGO-BGO, BGO-Ge(Exogam) and BGO-Ge(Gasp) on a common time scale. Right hand side: time prompt peak corresponding to time-differences between one (red dashed line) and all Ge-Ge pairs ("+" symbols).

The time calibration was based on the master clock frequency of 100 MHz making the difference between two rising edges of the clock (time stamps) to be exactly 10 ns. To illustrate the quality of the time measurement with EXILL we show in the left-hand side of figure 13 a doubly-gated, t_1-t_2 time-difference spectrum obtained from the ^{235}U(n,f) data, with the first gate set on the 2322 keV line above the 6^+ isomer in ^{134}Te, providing the start-time, t_1, and the second gate set on the 1279, 297 and 115 keV lines below the isomer, providing the delayed time, t_2. A clear exponential decay is visible compared to the prompt-prompt t_1-t_2 time-difference spectrum, doubly gated on the prompt, 2322 and 549 keV lines above the isomer. In the right-hand side of figure 13 a fit of an exponential with constant background function is shown, resulting in the half-life of $T_{1/2}$ = 163.9(7) ns, which agrees well with the literature value of $T_{1/2}$ = 164.1(9) ns [55].

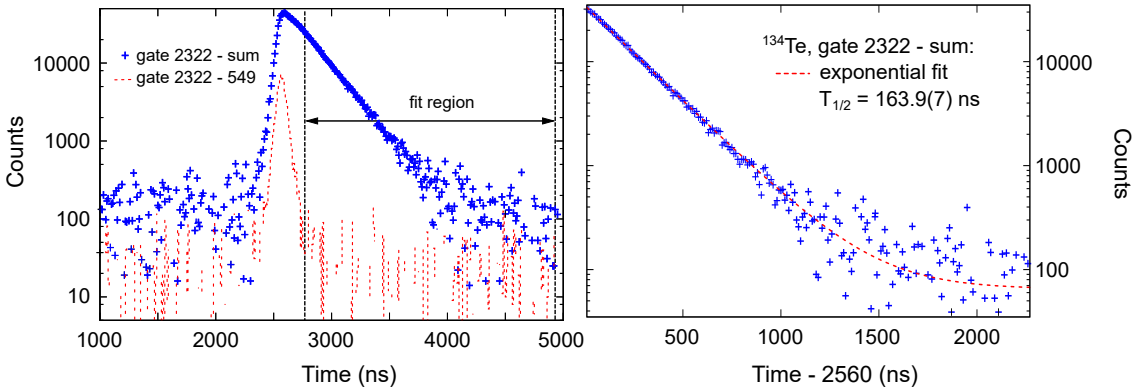

Figure 13. Left hand side: time-decay spectrum for the 6^+ isomer in ^{134}Te, doubly-gated on the 2322- and the sum of 1279, 297 and 115 keV lines of ^{134}Te (crosses); time-prompt spectrum doubly-gated on the 2322 and 549 keV lines of ^{134}Te (dashed line). Time "zero" is at 2560 ns. Right hand side: an exponent-plus-constant-background fit to the time-decay spectrum of the left-hand figure, performed in the shown region.

2017 JINST 12 P11003

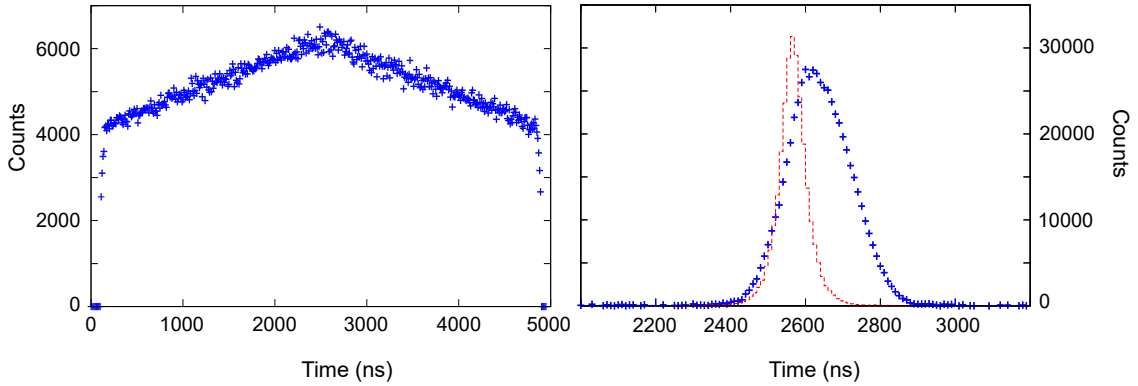

Figure 14. Left hand side: time-difference spectrum doubly-gated on the 2223 keV line from the ^{1}H(n,γ) reaction. Right hand side: prompt-time spectra doubly gated on lines from the ^{27}Al(n,γ) capture reaction (dashed red line gating on 2959 and 4734 keV, "+"-symbols gating on 2959 and 31 keV).

We note that the triggerless data from EXILL allow the study of isomers also in a micro-second range. However, as explained in ref. [56] specific corrections may be needed for long half lives ($T_{1/2} > 1\,\mu$s), due to the fact that reaction events occur randomly in time. This is illustrated in the left-hand side of figure 14 where we show a time-difference spectrum doubly gated on the prompt, 2223 keV line from the ^{1}H(n,γ) capture reaction, which was a very strong single line in all our measurements. The spectrum shows the time difference between two subsequent ^{1}H(n,γ) capture reactions, for which the 2223 keV line was registered by EXILL. It is clearly seen that events occuring randomly in time at high rate can produce a pronounced time "slope", which is related to the event rate. This applies also to pairs of γ-lines in coincidence.

Analogously, for short half lives ($T_{1/2} < 100$ ns) one needs to correct for the finite width of the prompt peak via the usual unfolding procedure. The position, the shape and the width of the "prompt" peak depend strongly on the γ-energy, due to energy dependence of γ-ray interaction as well as the specific properties of the data acquisition algorithm. The right-hand side of figure 14 illustrates this for pairs of lines from the 4734-2959-31 keV γ-cascade following the ^{27}Al(n,γ) capture reaction. The narrow prompt peak (dashed line) results from gating on two high-energy lines, 2959 and 4734 keV. The double gate on the 2959 and 31 keV lines produces a much broader "prompt" peak, for the low electric signal produced in the Ge crystal by the 31 keV γ-ray.

In figure 15 we demonstrate the broadening of the prompt time peak to be independent of the count rate of the Ge detectors. The figure compares the prompt time peak for the 815–977 keV cascade in ^{96}Sr, measured in ^{235}U(n,f) at about 600 kHz event rate to the prompt time peak for the 847–884 keV cascade in ^{134}Xe populated in beta decay of ^{134}I, measured at about 60 kHz rate after the ^{235}U(n,f) run. There is no difference between the widths of the two time prompt peaks, despite very different data rates.

7.2 Angular correlations

The high symmetry of the EXILL germanium detector array (rhombicuboctahedron) allows for a very effective angular correlation measurement at four relative angles between the detectors, 0°, 45°, 60° and 90°. It is worth noting that the four angles are the only angles between any pair of

2017 JINST 12 P11003

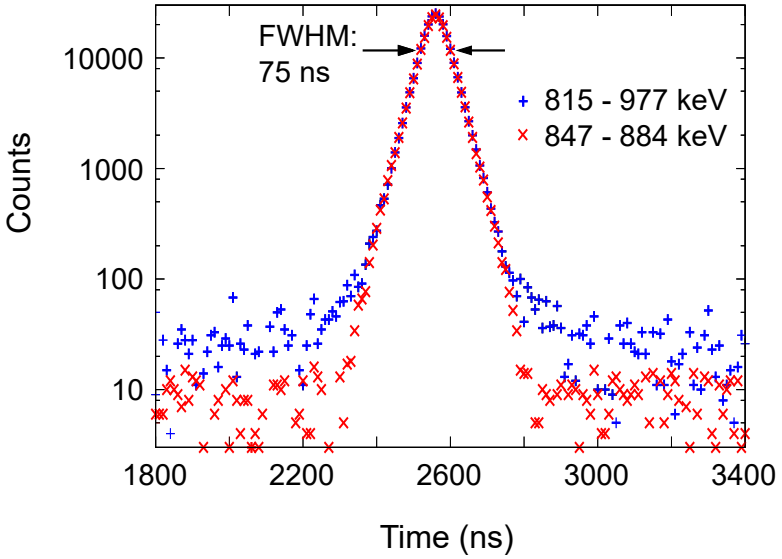

Figure 15. The prompt time peak for the 815–977 keV cascade in ^{96}Sr measured in ^{235}U(n,f) ("+" symbols) at 600 kHz event rate compared to the 847–884 keV cascade at 60 kHz rate ("×" symbols) populated in the β-decay of ^{134}I and measured after the ^{235}U(n,f) run.

Ge-detectors in the array taking into account the symmetry of angular correlation formulas with respect to 90°. Here the EXOGAM Clovers, used in add-back mode, were considered as a single detector. In the following we discuss the angular-correlation analysis for three angles, only, using data from a subset of the EXILL array - the eight EXOGAM detectors placed in one plane in an octagonal geometry perpendicular to the neutron beam. We have chosen this option due to the fact that the eight EXOGAM detectors are very similar to each other, with almost identical efficiencies and geometrical properties, which lowers the need for possible instrumental corrections, while GASP and Lohengrin detectors had rather different properties.

The present analysis of angular correlations is based on the theory of angular correlations as presented in ref. [57], including the convention of the sign for the mixing coefficient, δ, adopted there. The theoretical formula for the angular correlation function between two consecutive transitions γ_1 and γ_2 in a cascade emitted from an unoriented state with spin J_1, through an intermediate state with spin J_2 to the final level with J_3 can be expanded into a series of Legendre polynomials

$$W(\theta) = A_0 \sum_k a_k P_k(cos\theta). \tag{7.3}$$

Here, θ is the angle between the two γ-rays, P_k are the Legendre polynomials, k is an even integer number going from zero to the least of $2J_2$, $2L_1$ or $2L_2$, where L_1 and L_2 are the maximum multipolarities of γ_1 and γ_2, respectively. The value of A_0 is a common scaling factor describing the intensity of the cascade and linking the coefficients $a_k = A_k/A_0$ to the angular correlation coefficients A_k. To a large extent the procedure and formulas for deriving the coefficients a_k are published in [3]. Within this procedure the specific EXILL detector geometry and its size is represented by normalized attenuation coefficients q_k calculated using an opening angle of $\alpha = 18(1)°$ yielding the values $q_2 = 0.86(2)$ and $q_4 = 0.60(3)$.

2017 JINST 12 P11003

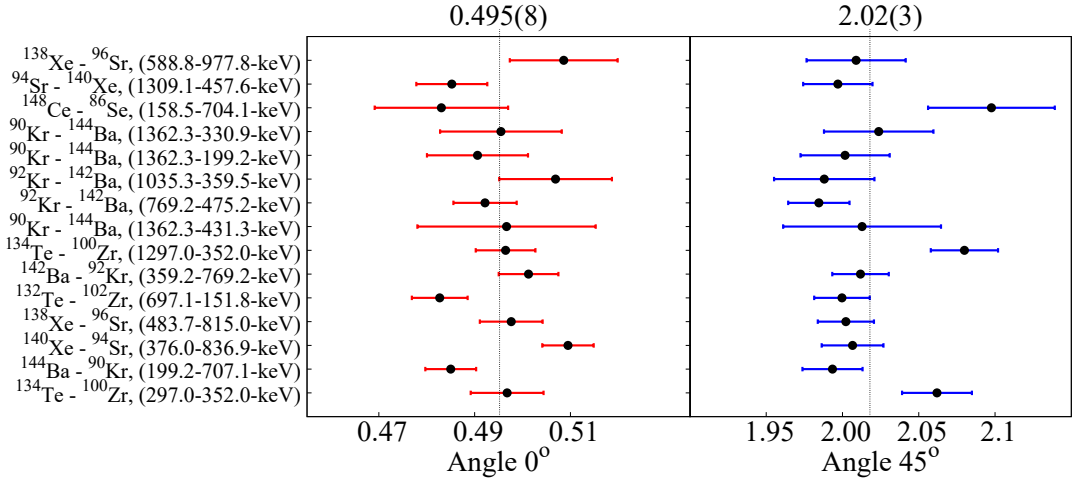

Figure 16. Determination of the normalization coefficients $n(\theta)$ from uncorrelated γ-rays in ^{235}U(n,f). The respective fission fragments and γ-energies are given on the left-hand side.

To extract experimental angular correlations with three angles, we have sorted three different γ coincidence matrices, each corresponding to one of the 0°, 45° and 90° angles between the two γ-rays. In the "octagon" setup considered, there were 4, 16 and 8 independent detector pairs contributing to the angles 0°, 45° and 90° respectively and the $\gamma\gamma$-coincidences need to be re-normalized respectively by introducing normalization coefficients $n(\theta)$. Accounting for different numbers of pairs as well as some differences between the efficiencies of the Ge detectors, these normalization factors may differ slightly from pure geometrical calculations, so that they have to be determined experimentally.

For the experimental determination of the normalization coefficients, $n(\theta)$, it was required for the normalized intensity distribution $N_{\gamma\gamma}(\theta)/n(\theta)$ to be independent of θ for cascades of two uncorrelated γ-rays. An example of such a cascade in our measurement are the two γ-rays emitted by two fission fragments, one γ from one fragment and the other from its fission-partner fragment. The discussed determination of the $n(\theta)$ coefficients does not require any knowledge of the q_k coefficients. For the convenience of graphical representations, the experimental data were always normalized to 1 at an angle $\theta = 90°$. Consequently, the $n(90°)$ coefficient is exactly 1, while its error was included in the errors of the other $n(\theta)$ coefficients.

In figure 16 we show an example of the determination of $n(\theta)$ based on 15 uncorrelated cascades of two γ-rays from the partner fission fragments from ^{235}U(n,f), which are indicated on the left-hand side of the plot. The analysis yields $n(0°) = 0.495(8)$ and $n(45°) = 2.02(3)$. Analysis of further uncorrelated cascades from other measurements of the EXILL campaign, with the same detector setup, and cascades with zero anisotropy (for instance the $2 \rightarrow 0 \rightarrow 2$ cascades in even-even nuclei) provided consistent results and allowed to obtain more precise average values of $n(0°) = 0.495(4)$ and $n(45°) = 2.011(8)$, which are recommended for further analysis of three-angle correlations with this setup.

With the experimentally determined $n(\theta)$ coefficients a refined adjustment of the q_k attenuation coefficients is possible by fitting them to experimental angular correlations for known cascades, preferably with large a_k coefficients (for example $0 \rightarrow 2 \rightarrow 0$ cascades in even-even nuclei). An

2017 JINST 12 P11003

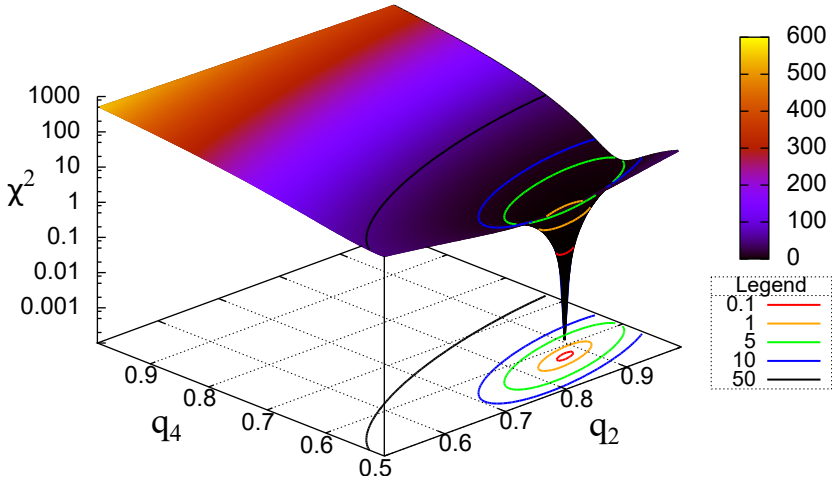

Figure 17. A χ^2 analysis for (q_2, q_4) with the 448-934 keV cascade in ^{92}Zr.

example of such analysis is shown in figure 17 for the highly anisotropic 448-934 keV cascade in ^{92}Zr, populated by ^{91}Zr(n,γ) reactions on the Zr-backing of the ^{235}U target, with spins 0, 2 and 0 of the initial, intermediate and final states, respectively (for such a cascade the theoretical a_2 and a_4 coefficients are 0.357 and 1.143, respectively). The formula fitted in figure 16 reads:

$$\chi^2(q_2, q_4) = \left(\frac{W_{\rm exp}(0^\circ) - W_{\rm th}(0^\circ, q_2, q_4)}{\Delta W_{\rm exp}(0^\circ)}\right)^2 + \left(\frac{W_{\rm exp}(45^\circ) - W_{\rm th}(45^\circ, q_2, q_4)}{\Delta W_{\rm exp}(45^\circ)}\right)^2$$

The above χ^2 analysis points distinctively to $q_2 = 0.870$ and $q_4 = 0.575$, in good agreement with the calculation based on the solid angle estimates of the EXOGAM Clover detectors. Typically the error estimate would be extracted from a countour equal to $\chi^2_{\rm min}$+1.0. In the present work two q_k coefficients are fitted to two experimental points and the fit is "exact" (zero degrees of freedom); the χ^2 minimum reaches zero. Still the $\chi^2_{\rm min}$ + 1.0 approach gives a reasonable estimate of the uncertainties $\Delta q_2 = 0.03$ and $\Delta q_4 = 0.02$, which is consistent with the error estimates obtained from direct calculations according to [3].

With the normalization and attenuation coefficients precisely determined, as described above, we have tested the angular correlation analysis for several known cases. Results are shown in table 5 and in figure 18 for four characteristic angular correlations: (a) two stretched quadrupole-quadrupole and quadrupole-dipole transitions in a cascade and (b) strongly anisotropic (0-2-0) versus isotropic (934–511 keV) correlations from β-decay.

For cascades of non-stretched transitions, which can be mixtures of two multipolarities, a more advanced type of analysis has to be performed. A very common situation is the combination of a known transition and an unknown transition, which is a mixture of two multipolarities with the mixing coefficients δ. To determine the δ coefficient the $A_k(\delta)$ coefficients are calculated for a given spin and multipolarity hypothesis as a function of δ. Then the $A_k(\delta)$ values are compared against the experimentally determined A_k^{exp} values applying the χ^2 test.

In figure 19 and table 5 we show examples of such an analysis for two M1+E2 mixed transitions in the ^{92}Zr nucleus. In figure 19(a) we show the χ^2 test for the 1132.1-934.5 keV cascade. The experimental (A_2, A_4) values (blue box in the upper pannel of figure 19(a)) shown against the $A_2(\delta)$

2017 JINST 12 P11003

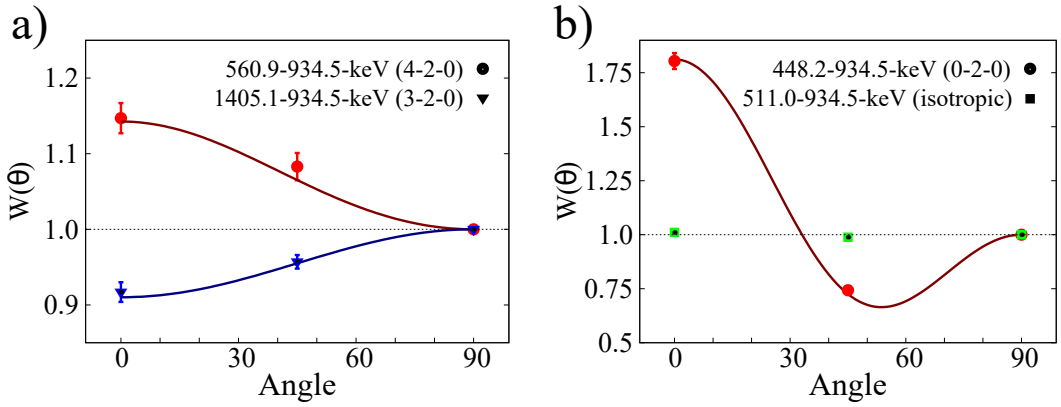

Figure 18. Angular correlations for strong γ-cascades in ^{92}Zr, populated by neutron capture on the Zr backing of the first ^{235}U(n,f) target. In figure b), the error bars are smaller than the size of the symbols. The point at 90° is at 1 by definition. Note that the 511 keV was produced by a β-decaying nucleus, while the neutron beam was off.

Table 5. Experimental and theoretical angular correlation coefficients measured for transitions in ^{92}Zr populated by neutron capture. First three lines: pure, stretched transitions. Fourth line: isotropic (511 keV) transitions. Last two lines: mixed transitions.

$\gamma_1 - \gamma_2$ (keV)	J_1, J_2, J_3	a_2^{exp}	a_4^{exp}	a_2^{th}	a_4^{th}	$\delta(\gamma_1)$
560.9 - 934.5	4 - 2 - 0	0.106(12)	−0.012(30)	0.102	0.009	0.00
1405.1 - 934.5	3 - 2 - 0	−0.068(8)	0.008(17)	−0.071	0.000	0.00
448.2 - 934.5	0 - 2 - 0	0.356(21)	1.120(41)	0.357	1.143	0.00
511.0 - 934.5	isotropic	0.006(12)	0.012(24)	0.000	0.000	0.00
1132.1 - 934.5	2 - 2 - 0	0.191(19)	0.295(40)			−2.824(23)
912.7 - 934.5	2 - 2 - 0	0.255(11)	−0.001(25)			−0.007(17)

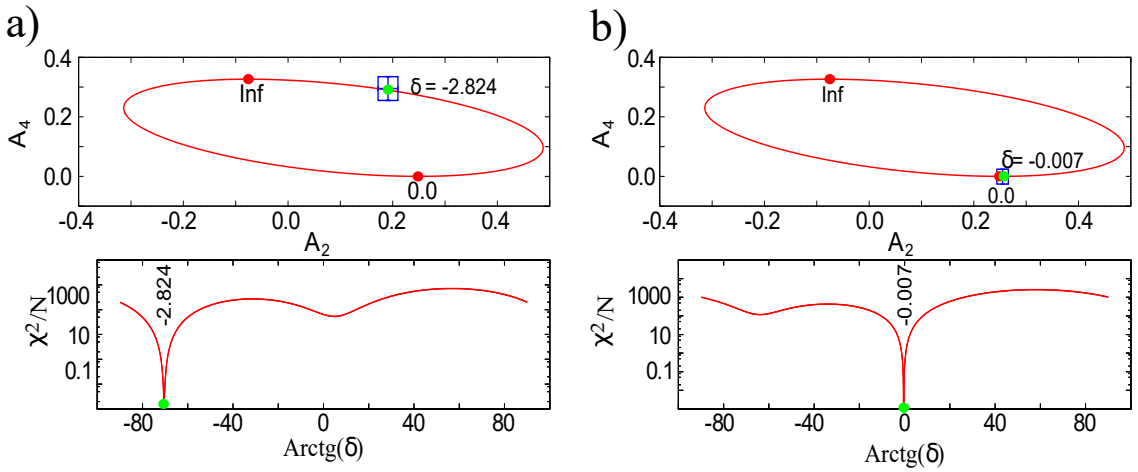

Figure 19. The χ^2 analysis for a) the 1132.1-934.5 keV cascade and b) the 912.7-934.5 keV cascade in ^{92}Zr, populated by neutron capture. See text for details.

$A_4(\delta)$ values for the 2-2-0 spin hypothesis in the cascade (the red ellipse), provide one solution with δ = -2.824(23) for the 1132.1 keV transition in ^{92}Zr, as shown by the χ^2 test in the lower pannel of figure 19(a). This result agrees with and is more precise than the evaluated value of $\delta = -3.2(^{0.5}_{0.4})$ [58].

In figure 19(b) the χ^2 test for the 912.7-934.5 keV cascade provides the mixing ratio δ = -0.007(17) for the 912.7 keV transition in ^{92}Zr, which agrees with and is more precise than the published value $\delta = -0.002(25)$ [58].

The results presented in figures 18, 19 and table 5 indicate that with the present "octagon" subset of the EXILL detectors very precise angular correlations can be obtained. With the three angles the angular correlation analysis is possible for $\gamma\gamma$-cascades, where at least one of the transitions has a dipole or quadrupole multipolarity, while the other one can have any multipolarity.

In order to analyze angular correlations for $\gamma\gamma$-cascades, where both transitions have multipolarities higher than quadrupole, more angles are needed for analysis. The four angles provided by the EXILL array allow the investigation of angular correlations for cascades where one of the transitions has a multipolarity not higher than octupole, while the other can have any multipolarity. The four-angle setup has also the advantage of higher statistics - the number of detector pairs contributing to the four angles, 0°, 45°, 60° and 90° are 8, 32, 48 and 32, respectively. However, because different types of detectors with rather different efficiencies were used in EXILL (eight EXOGAM Clovers, two LOHENGRIN Clovers and 6 GASP coaxial detectors), both the $n(\theta)$ normalization coefficients and the q_k attenuation coefficients have to be determined specifically. Such, an analysis would surpass the rather general character of this paper and will be published elsewhere.

8 Summary and perspectives

The field of γ-ray spectroscopy based on neutron-induced reactions is an important part of nuclear physics where many interesting results can be obtained when using efficient arrays of Ge detectors. In this paper we have presented EXILL, an efficient detector array for precise measurements of γ-rays from neutron-capture and neutron-induced fission. The array, placed at the cold neutron beam facility PF1B of ILL Grenoble, consisted of up to 49 germanium crystals mounted in a rhombicuboctahedron geometry. The high efficiency and granularity of the array allows measurements of multi-fold γ-coincidences. The neutron collimation of the setup provided a neutron beam of about 1 cm in diameter and a thermal neutron-capture equivalent flux of about 1×10^8 n cm^{-2} s^{-1} at the target position, with negligible neutron halo. The background level is acceptable and no effect of neutron induced damage on the Ge detectors has been observed. Due to a fast digital acquisition system the detector array collected up to 6×10^5 triggerless single γ-events per second. The triggerless data offer the possibility to measure various time correlations and half-lives of excited levels in the nano- to micro-second range (if combined with $LaBr_3$:Ce detectors down to picosecond range) with high accuracy [15]. Precise energy and efficiency calibrations of EXILL in the energy range from 30 keV up to 10 MeV were performed using standard calibration sources of ^{133}Ba, ^{60}Co and ^{152}Eu as well as transitions from the reactions ^{27}Al$(n,\gamma)^{28}$Al and ^{35}Cl$(n,\gamma)^{36}$Cl. The data from these reactions have shown that with this setup the neutron binding energies can be determined with an accuracy down to the eV level while γ-ray angular correlations can be measured with the precision down to the percent level. Further — not detailed in this paper — due to the use

2017 JINST 12 P11003

of Clover detectors the linear polarization of γ-rays could be determined with a precision down to the 10% percent level (which will be subject of an individual publication).

The described setup has been used to measure γ-rays from (n,γ) reactions for several target nuclei. A so-far-preliminary comparison with data from previous (n,γ) measurements shows that there should be many more nuclei, for which much improved information on nuclear structure could be obtained if further (n,γ) experiments with the present setup will be carried out in the future. Similarly, measurements of prompt γ-rays from fission products of ^{235}U(n,f) and ^{241}Pu(n,f) performed with EXILL delivered unique data sets for neutron-rich nuclei. Using triple coincidences on known transitions of fission products or their complementary partner it is possible to place individual γ-transitions in the level scheme of these isotopes. The analysis of this very rich data set is presently in progress.

The EXILL campaign has also been an important step forward towards the development of a future instrument at the ILL: the FIssion Product Prompt γ-ray Spectrometer (FIPPS) [59]. The FIPPS setup will represent a permanent extension of the temporary EXILL campaign. It aims at combining a high-resolution, high-efficiency germanium array and a large acceptance recoil spectrometer for mass determination. The subsequent improvement in the overall resolving power will allow the identification of new, weak γ-rays. A variety of alternative targets for neutron-induced fission (^{233}U, ^{239}Pu, ^{242m}Am, ^{243}Cm, ^{245}Cm, ^{247}Cm, ^{249}Cf, ^{251}Cf) can be exploited. This will considerably extend the number of nuclei accessible for nuclear structure studies. Specific setups including other ancillary devices as plungers [60] or magnets for g-factor [19, 20] measurements will provide more detailed nuclear structure information.

Acknowledgments

We are grateful to Didier Berruyer (ILL), Thomas Brenner (ILL), Mathieu Guigou (ILL), Norbert Laurens (ILL) , Laurent Ménager (GANIL), Jean Ropert (GANIL), Johann Menu (LPSC), Sebastian Roudier (LPSC), Jean-Claude Malacour (LPSC), Sam Roni (LPSC), Calogero Geraci (LPSC) for their support in the design, construction and setup of the experiment. We thank the ILL IT-service, Catherine Biscarat (LPSC) and Bernard Boutherin (LPSC), the CCIN2P3 in particular Yonny Cardenas, Pascal Calvat and Jean-Yves Nief for helping and providing support in data transfer and storage. A special thank goes to Frank Rey, Emilio Ruez-Martinez, Silvain Sallaz-Damaz for setting up the electronics. We thank Franz M. Wagner (MEDAPP instrument at FRM2, Garching) for providing the Gafchromic film for testing the neutron beam alignment.

This work has been partly supported by the Polish National Science Centre under contract DEC-2013/09/B/ST2/03485, the U.S. DOE grant No. DE-FG02-91ER40609, the NUPNET and the German BMBF under contracts O5P12PKNUF, 05P15RDFN1 and 05P12RDNUP and the German DFG contract KR 1796/2-1.

References

[1] J. Eberth and J. Simpson, *From Ge(Li) detectors to gamma-ray tracking arrays: 50 years of gamma spectroscopy with germanium detectors*, *Prog. Part. Nucl. Phys.* **60** (2008) 283.

2017 JINST 12 P11003

[2] R.L. Gill, R.F. Casten, W.R. Phillips, B.J. Varley, C.J. Lister, J.L. Durell et al., *New levels in Er-168: Use of a Compton-suppressed Ge array with the (n, gamma) reaction*, *Phys. Rev.* **C 54** (1996) 2276.

[3] W. Urban et al., *New instrumentation for precise (n,γ) measurements at ILL Grenoble*, 2013 *JINST* **8** P03014.

[4] C. Bernards, W. Urban, M. Jentschel, B. Markisch, J. Jolie, C. Fransen et al., *gamma gamma angular-correlation analysis of Hg-200 after cold-neutron capture*, *Phys. Rev.* **C 84** (2011) 047304.

[5] I. Ahmad and W.R. Phillips, *Gamma rays from fission fragments*, *Rep. Prog. Phys.* **58** (1995) 1415.

[6] J.H. Hamilton et al., *New insights from studies of spontaneous fission with large detector arrays*, *Prog. Part. Nucl. Phys.* **35** (1995) 635.

[7] I.Y. Lee, *Physics with GAMMASPHERE and beyond*, *Prog. Part. Nucl. Phys.* **38** (1997) 65.

[8] M.A. Kellett, O. Bernillon and R.W. Mills, *The Jeff-31/6311 radioactive decay data and fission yields sub-libraries Jeff report 20*, Nuclear Energy Agency, (2009).

[9] G.S. Simpson, J.C. Angelique, J. Genevey, J.A. Pinston, A. Covello, A. Gargano et al., *New information on excited states below the mus isomer in Sb-136*, *Phys. Rev.* **C 76** (2007) 041303.

[10] G.S. Simpson et al., *Near-yrast, medium-spin, excited states of Rb-91, Rb-93 and Rb-95*, *Phys. Rev.* **C 82** (2010) 024302.

[11] H.R. Koch, H.G. Börner, J.A.Pinston et al., *The curved crystal gamma ray spectrometers "GAMS 1, GAMS 2, GAMS 3" for high resolution (n, γ) measurements at the high flux reactor in Grenoble*, *Nucl. Instrum. Meth.* **175** (1980) 401.

[12] F. Hoyler et al., *Spectroscopy of the ODD-ODD nucleus 76 As and its supersymmetric description*, *Nucl. Phys.* **A 512** (1990) 189.

[13] W. Ritz, *On a New Law of Series Spectra*, *Astrophys. J.* **28** (1908) 237.

[14] W.F. Davidson et al., *Identification of all intrinsic excitations below 2 MeV in* ^{168}*Er*, *J. Phys.* **G 7** (1981) 455.

[15] J.M. Régis et al., *Germanium-gated γ-γ fast timing of excited states in fission fragments using the EXILL&FATIMA spectrometer*, *Nucl. Instrum. Meth.* **A 763** (2014) 210.

[16] A. G. Smith et al., *Lifetimes in Neutron-Rich Nd Isotopes Measured by a Doppler Profile Method*, *Phys. Rev. Lett.* **73** (1994) 2540.

[17] GANDS95 collaboration, A.V. Ramayya et al., *Observation of Be-10 Emission in the Cold Ternary Spontaneous Fission of Cf-252*, *Phys. Rev. Lett.* **81** (1998) 947.

[18] A.G. Smith et al., *Correlated spins of complementary fragment pairs in the spontaneous fission of Cf-252*, *Phys. Rev.* **C 60** (1999) 064611.

[19] A.G. Smith et al., *Measurements of g-factors of excited states in Ba and Ce nuclei using γ rays from secondary fission fragments*, *Phys. Lett.* **B 453** (1999) 206.

[20] C. Goodin et al., *g factors, spin-parity assignments and multipole mixing ratios of excited states in* $N = 82$ *isotones Te-134, I-135*, *Phys. Rev.* **C 78** (2008) 044331.

[21] H. Häse et al., *A long ballistic supermirror guide for cold neutrons at ILL*, *Nucl. Instrum. Meth.* **A 485** (2002) 453.

[22] H. Abele et al., *Characterization of a ballistic supermirror neutron guide*, *Nucl. Instrum. Meth.* **A 562** (2006) 407 [nucl-ex/0510072].

2017 JINST 12 P11003

[23] K. Lefmann and K. Nielsen, *McStas, a general software package for neutron ray-tracing simulations*, *Neutron News* **10** (1999) 20.

[24] P. Willendrup, E. Farhi and K. Lefmann, *McStas 1.7 — a new version of the flexible Monte Carlo neutron scattering package*, *Physica* **B 350** (2004) E735.

[25] G. Bocchi et al., *Study of Low-spin States in Ca Isotopes via Neutron Capture Reactions*, *Acta Phys. Polon.* **B 46** (2015) 647.

[26] P. Bączyk et al., *High precision γ spectroscopy of 69,71Zn from (n, γ) reactions using EXILL*, *EPJ Web Conf.* **93** (2015) 01042.

[27] C. Lorenz et al., *Neutron-capture experiment on 77Se with EXILL at ILL Grenoble*, *EPJ Web Conf.* **93** (2015) 01050.

[28] M. Thürauf et al., *Identification of low-energy isovector octupole states in* ^{144}Nd, *J. Phys. Conf. Ser.* **724** (2016) 012050.

[29] M. Jentschel, L. Sengele, D. Curien, J. Dudek and F. Haas, *The Negative Parity Bands in* ^{156}Gd, *Phys. Scripta* **89** (2014) 054017 [arXiv:1404.5794].

[30] J. Jolie et al., *The (n,γ) campaigns at EXILL*, *EPJ Web Conf.* **93** (2015) 01014.

[31] J. Jolie et al., *Test of the* SO(6) *selection rule in* ^{196}Pt *using cold-neutron capture*, *Nucl. Phys.* **A 934** (2015) 1.

[32] N. Cieplicka-Oryńczak et al., *Multipolarity of the* $2^- \rightarrow 1^-$ *, ground-state transition in Bi210 via multivariable angular correlation analysis*, *Phys. Rev.* **C 94** (2016) 014311.

[33] N. Cieplicka-Oryńczak et al., *Approaching complete low-spin spectroscopy of* ^{210}Bi *with a cold-neutron capture reaction*, *Phys. Rev.* **C 93** (2016) 054302.

[34] P. Bączyk et al., *Near-yrast excitations in nucleus* ^{83}As*: Tracing the* $\pi g_{9/2}$ *orbital in the* ^{78}Ni *region*, *Phys. Rev.* **C 91** (2015) 047302.

[35] M. Czerwiński et al., *Neutron-proton multiplets in the nucleus* ^{88}Br, *Phys. Rev.* **C 92** (2015) 014328.

[36] M. Czerwiński et al., *Neutron-proton multiplets in the odd-odd nucleus* $^{90}_{37}Rb_{53}$, *Phys. Rev.* **C 93** (2016) 034318.

[37] S. Ilieva et al., *Measurement of picosecond lifetimes in neutron-rich Xe isotopes*, *Phys. Rev.* **C 94** (2016) 034302.

[38] W. Urban et al., *Low-spin structure of* $^{86}_{35}Br_{51}$ *and* $^{86}_{36}Kr_{50}$ *nuclei: The role of the* $g_{7/2}$ *neutron orbital*, *Phys. Rev.* **C 94** (2016) 044328.

[39] P. Spagnoletti et al., *Half-life of the* $15/2^+$ *state of* ^{135}I*: A test of* $E2$ *seniority relations*, *Phys. Rev.* **C 95** (2017) 021302.

[40] L. W. Iskra et al., *New isomer in* ^{96}Y *marking the onset of deformation at* $N = 57$, *EPL* **117** (2017) 12001.

[41] L.V. Drapchinsky, T.E. Kuzmina and S.M. Soloviev, *Practice of using the multiple painting method*, *Nucl. Instrum. Meth.* **A 438** (1999) 116.

[42] J. Runke et al., *Preparation of actinide targets for the synthesis of the heaviest elements*, *J. Radioanal. Nucl. Chem.* **299** (2014) 1081.

[43] http://pro.ganil-spiral2.eu/laboratory/detectors/exogam.

[44] F. Azaiez, *EXOGAM: a γ-ray spectrometer for radioactive beams*, *Nucl. Phys.* **A 654** (1999) 1003.

2017 JINST 12 P11003

[45] J. Simpson et al., *The EXOGAM array: A radioactive beam gamma-ray spectrometer*, *Acta Phys. Hung. New Ser. Heavy Ion Phys.* **11** (2000) 159.

[46] http://npgroup.pd.infn.it/GASP/

[47] C. Rossi Alvarez, *The GASP array*, *Nucl. Phys. News* **3** (1993) 10.

[48] G. Duchêne et al., *The Clover: a new generation of composite Ge detectors*, *Nucl. Instrum. Meth.* **A 432** (1999) 90.

[49] CAEN, *Technical information manual mod. V1724 8 channel 14 bit 100 MS/s digitiser*, Italy (2010), http://www.caen.it.

[50] CES, *RIO3 8064 powerpc-based VMEx-LI processor board user manual DOC 8064/UM version 3.4*, Switzerland (2003), https://www.mrcy.com/mission-computing-safety-dal/.

[51] V.T. Jordanov and G.F. Knoll, *Digital synthesis of pulse shapes in real time for high resolution radiation spectroscopy Nucl. Instrum. Meth.* **A 345** (1994) 337.

[52] https://irods.org/.

[53] A.F. Sánchez-Reyes, M.I. Febrián, J. Baró, J. Tejada, *Absolute efficiency calibration function for the energy range 63–3054 keV for a coaxial Ge(Li) detector*, *Nucl. Instrum. Meth.* **B 28** (1987) 123.

[54] K. Debertin and R.G. Helmer, *Gamma- and X-ray Spectromety with Semiconductor Detectors*, Elsevier Science Publishers B.V. (1988).

[55] A.A. Sonzogni, *Nuclear Data Sheets for A = 134*, *Nucl. Data Sheets* **103** (2004) 1.

[56] W. Urban et al., *New isomers and medium-spin structure of the Y-95 nucleus*, *Phys. Rev.* **C 79** (2009) 044304.

[57] K.S. Krane, R.M. Steffen, R.M. Wheeler, *Directional correlations of gamma radiations emitted from nuclear states oriented by nuclear reactions or cryogenic methods*, *Atom. Data Nucl. Data* **11** (1973) 351.

[58] C.M. Baglin, *Nuclear Data Sheets for A = 92*, *Nucl. Data Sheets* **113** (2012) 2187.

[59] A. Blanc, A. Chebboubi, H. Faust, M. Jentschel, G. Kessedjian, U. Köster et al., *FIssion Product Prompt γ-ray spectrometer: Development of an instrumented gas-filled magnetic spectrometer at the ILL*, *Nucl. Instrum. Meth.* **B 317** (2013) 333.

[60] G. Mamane, E. Cheifetz, E. Dafni, A. Zemel and J.B. Wilhelmy, *Lifetime measurements of excited levels in prompt fission products of 252 Cf*, *Nucl. Phys.* **A 454** (1986) 213.

2017 JINST 12 P11003